CRASH3: cosmological radiative transfer through metals

L. Graziani[1] *, A. Maselli[2], B. Ciardi[1]

[1] *Max-Planck-Institut für Astrophysik, Karl-Schwarzschild-Straße 1, D-85748 Garching b. München, Germany*
[2] *EVENT Lab for Neuroscience and Technology, Universitat de Barcelona, Passeig de la Vall d'Hebron 171, 08035 Barcelona, Spain*

ABSTRACT
Here we introduce CRASH3, the latest release of the 3D radiative transfer code CRASH. In its current implementation CRASH3 integrates into the reference algorithm the code Cloudy to evaluate the ionisation states of metals, self-consistently with the radiative transfer through H and He. The feedback of the heavy elements on the calculation of the gas temperature is also taken into account, making of CRASH3 the first 3D code for cosmological applications which treats self-consistently the radiative transfer through an inhomogeneous distribution of metal enriched gas with an arbitrary number of point sources and/or a background radiation. The code has been tested in idealized configurations, as well as in a more realistic case of multiple sources embedded in a polluted cosmic web. Through these validation tests the new method has been proven to be numerically stable and convergent. We have studied the dependence of the results on a number of physical quantities such as the source characteristics (spectral range and shape, intensity), the metal composition, the gas number density and metallicity.

Key words: Cosmology: theory - Radiative transfer - IGM

1 INTRODUCTION

During the last decade, observational and theoretical studies constraining the nature of the intergalactic medium (IGM) have shown that metals are a pervasive component of the baryonic budget of our universe and that they are associated with a wide range of hydrogen column density (N_{HI}) systems typically identified in quasars (QSO) absorption spectra at different redshift (Meyer and York 1987; Lu 1991; Songaila and Cowie 1996; Cowie and Songaila 1998; Ellison et al. 2000; Songaila 2001; Schaye et al. 2000, 2003; Aracil et al. 2004; Pieri et al. 2004; Becker et al. 2011; also see Meiksin 2009 for a review).

High H I column density absorbers, with $N_{HI} \geqslant 2 \cdot 10^{20} \mathrm{cm}^{-2}$, are easily identified in these spectra for the presence of strong damping wings, and are classified as Damped Lyα systems (DLAs). Column densities in the range $1.6 \cdot 10^{17} \, \mathrm{cm}^{-2} \leqslant N_{HI} \leqslant 10^{20} \, \mathrm{cm}^{-2}$ are instead associated with Lyman Limit Systems (LLSs) and spectroscopically identified by their strongly saturated Lyα lines. Both systems show C IV lines as well as many ions in lower ionisation states (Mn II, Si II, Fe II), and are typically associated with metallicities of $Z \sim 10^{-2} Z_\odot$ (LLSs; e.g. Steidel 1990) and $10^{-2} Z_\odot \leqslant Z \leqslant 0.3 Z_\odot$ (DLAs; e.g. Steidel 1990; Hellsten et al. 1997; Rauch et al. 1997; Pettini et al. 1999; Kulkarni et al. 2005).

The presence of metals in LLSs and DLAs can be interpreted as a natural product of the stellar nucleosynthesis acting therein. LLSs are in fact identified as clouds in the galactic halos, while high redshift ($z \sim 3$) DLAs are believed to be the progenitors of the present-day galaxies.

Advances in high resolution spectroscopy revealed weak metal absorption lines in the Lyα forest ($N_{HI} \lesssim 10^{-17}$ cm^{-2}), with C IV detected in most of the systems with $N_{HI} \geqslant 10^{15}$cm^{-2} and in more than half of the systems with $N_{HI} \geqslant 10^{14}$cm^{-2} (Tytler et al. 1995; Songaila and Cowie 1996). The typical metallicities of the Lyα forest are estimated in the range $10^{-4} Z_\odot \leqslant Z \leqslant 10^{-2} Z_\odot$ (Simcoe et al. 2004). The subsequent discovery of a metallic component in less dense regions (Cowie and Songaila 1998; Ellison et al. 2000; Schaye et al. 2000, 2003; Aracil et al. 2004; Pieri et al. 2004) has been interpreted as the evidence of efficient spreading mechanisms which are able to transport the metals far away from their production sites and pollute low density regions.

The redshift evolution of the gas metallicity has been extensively investigated. In the redshift range $1.5 < z < 4$, C IV and Si IV doublets are the main tracers of the IGM metallicity, because their rest frame wavelength is larger than the Lyα and the lines cannot be confused with those of the forest. In this range the column density distribution of C IV seems to remain constant (Songaila 2001). Although a consensus has not been reached yet, a decline in the abundance of C IV above $z \sim 4.5$ is reported by different

* E-mail: lgmaxp@mpa-garching.mpg.de

groups (Ryan-Weber et al. 2009; Becker et al. 2009, 2011; Simcoe et al. 2011). The Si IV doublet $\lambda\lambda 1393.76, 1402.77$ Å has been investigated in QSO line surveys in the redshift range $1.5 < z < 5.5$. Songaila (2001) measured $\Omega_{Si\,IV}$, the Si IV mass density relative to the critical density, in the redshift range $2 < z < 5.5$, finding a roughly constant value in the range $2 < z < 4.5$ for absorbers with column densities $10^{13} \mathrm{cm}^{-2} \leqslant N_{Si\,IV} \leqslant 10^{15} \mathrm{cm}^{-2}$, while $\Omega_{Si\,IV}$ may have increased by an order of magnitude in $4.5 < z < 5.5$. These abundance trends have been confirmed by subsequent studies (Boksenberg et al. 2003; Songaila 2005; Scannapieco et al. 2006).

At higher redshifts, a critical diagnostic role could be played instead by ions with lower ionisation states like C II, Si II and O II, probing colder gas (Oh 2002; Furlanetto & Loeb 2003; Becker et al. 2011).

Below $z \sim 1$ a larger sample of data is available also for the oxygen component which is the major tracer of the IGM metallicity. The interested reader can find more information in the recent study of Cooksey et al. (2011), and references therein.

Beyond this general consensus, many observational data remain controversial, as well as their interpretation which is of primary importance, e.g. in constraining different enrichment scenarios. The metal abundance, the number of ionisation states and the distribution in space and time are still subjects of intense debate (see Petitjean 2001, 2005).

The theoretical interpretation of the data is of particular relevance because observations of metals in dense regions, where stellar nucleosynthesis is active, provide a record of the star formation history, while observations in the IGM can be a good indicator of the galactic winds efficiency, the velocity structure of the IGM and more in general of the enrichment mechanism (Gnedin and Ostriker 1997; Ferrara et al. 2000; Cen and Bryan 2001; Madau et al. 2001). In fact, different scenarios have been considered in the literature, as an early enrichment by the first generation of stars (Madau et al. 2001), a continuous enrichment (Gnedin and Ostriker 1997; Ferrara et al. 2000; Scannapieco et al. 2002), or a late enrichment coinciding with the star formation peak at $z \sim 2 - 4$ (Adelberger et al. 2002). In addition, the determination of metal abundances could also constrain the efficiency of the gas cooling function (Sutherland & Dopita 1993; Maio et al. 2007; Smith et al. 2008; Wiersma et al. 2009a) and the formation of massive galaxies (Thacker et al. 2002).

For these reasons, several theoretical schemes for metal production and spreading have been developed, based on both semi-analytic models (e.g. Scannapieco et al. 2002, 2006) and numerical simulations (Oppenheimer & Davé 2006; Dubois & Teyssier 2007; Wiersma et al. 2009b; Maio et al. 2010; Schaye et al. 2010; Shen et al. 2010; Tornatore et al. 2010; Wiersma et al. 2010; Maio et al. 2011; Wiersma et al. 2011). In the most advanced approaches the ionisation state of the metals is calculated assuming the presence of a uniform UV background, which is then used as energetic input for photo-ionisation codes computing the metal ionisation states at the equilibrium (Oppenheimer & Davé 2006; Oppenheimer et al. 2009, 2012). The results of this approach are affected by the uncertainties associated to the assumptions on the shape and intensity of the radiation field, which is not calculated self-

consistently from the radiative transfer across the inhomogeneous gas distribution. Many studies suggest in fact that shadowing, filtering and self-shielding induce deviations in the shape and intensity of the background with respect to models in which the effects of the radiative transfer are neglected (Maselli & Ferrara 2005 and references therein).

Fluctuations in the photo-ionisation rates as well as spatial deviations in the IGM temperature due to the inhomogeneity of the cosmic web support this view at least on scales of few co-moving Mpc (see Maselli & Ferrara 2005; Furlanetto 2009; Meiksin 2009 and references therein). On larger scales ($\sim 100h^{-1}$ Mpc co-moving) the source spatial distribution and their spectral variability could be an additional cause of variations in the UVB (Zuo 1992b,a; Meiksin and White 2003; Bolton & Viel 2011).

The fluctuations induced by radiative transfer effects could also be efficiently recorded in the ionisation state of the metals, because their rich electronic structure and atomic spectrum are more sensitive, compared to H and He, to the radiation field fluctuations (Oh 2002; Furlanetto & Loeb 2003; Furlanetto 2009).

Numerical schemes which solve the cosmological radiative transfer equation by applying different approximations are now quite mature and well tested (Iliev et al. 2006a, 2009 and references therein for an overview of the available codes) and are able to simulate complex scenarios involving large cosmological boxes and number of sources (e.g. Ciardi et al. 2003a,b; Iliev et al. 2006b; Trac and Cen 2007; McQuinn et al. 2009; Baek et al. 2010; Ciardi et al. 2012). Typically, these codes are restricted to the hydrogen chemistry, with only a few of them including a self-consistent treatment of the helium component, which is particularly relevant for a correct determination of the gas temperature (see e.g. Ciardi et al. 2012). None of them though includes the treatment of metal species.

In the interstellar medium (ISM) community, on the other hand, several photo-ionisation codes, as `Cloudy` (Ferland et al. 1998), `MAPPINGSIII` (Allen et al. 1998) and `MOCASSIN` (Ercolano et al. 2003) are able to simulate the complex physics of galactic HII regions largely polluted by heavy elements.

The aim of the present work is to describe a novel extension of the radiative transfer code `CRASH` (Ciardi et al. 2001; Maselli et al. 2003, 2009), which has been integrated with `Cloudy`, allowing the prediction of metal ionisation states self-consistently with the radiation field as calculated by the radiative transfer through the IGM density field.

The paper is structured as follows. In Section 2 and 3 we briefly introduce the radiative transfer code `CRASH` and the photo-ionisation code `Cloudy`. In Section 4 we illustrate the details of the integration of the two codes into a self-consistent pipeline. The tests of the new `CRASH` variant called `CRASH3` are reported in Section 5. Section 6 summarizes the conclusions.

2   CRASH

`CRASH` is a 3D radiative transfer (RT) code designed to follow the propagation of hydrogen ionising photons (i.e. with energy $E \geqslant 13.6$ eV) through a gas composed by H and He. The code adopts a combination of ray tracing and Monte

Carlo (MC) sampling techniques to propagate photon packets through an arbitrary gas distribution mapped on a cartesian grid, and to follow in each grid cell the evolution of gas ionisation and temperature. This treatment guarantees a reliable description of such evolution in a large variety of configurations, as shown by the Cosmological Radiative Transfer Comparison Project tests (Iliev et al. 2006a) and its various applications to the study of the H and He reionisation (Ciardi et al. 2003a,b, 2012), the imprints of the fluctuating background on the Lyα forest (Maselli & Ferrara 2005), the quasar proximity effects (Maselli et al. 2007, 2009) and the impact of reionisation on the visibility of Lyα emitters (Dayal et al. 2011; Jeeson-Daniel et al. 2012).

The MC algorithm adopted allows to easily add new physical processes. In its first version (Ciardi et al. 2001) the code describes H photo-ionisation due to point sources, and includes the effect of re-emission following gas recombination. The subsequent versions brought about significant improvements. First the physics of He and the thermal evolution of the gas have been introduced, together with the treatment of an ionising background field (Maselli et al. 2003; Maselli & Ferrara 2005). In the latest release (`CRASH2`; Maselli et al. 2009, hereafter MCK09) we introduced multi-frequency photon packets obtaining significant improvements in terms of accuracy of the ionisation and temperature profiles, as well as computational speed. Hereafter the code name `CRASH` will refer to the version `CRASH2`.

In parallel with the reference code, variants and extensions have been developed such as: MCLyα (Verhamme et al. 2006), which has adapted the reference algorithm to treat the resonant propagation of Lyα photons; `CRASH`α (Pierloni et al. 2009), which follows the self-consistent propagation of both Lyα photons and ionising continuum radiation; Partl et al. (2011) have instead developed an MPI parallel implementation of the base `CRASH` algorithm.

The new release described in this paper (hereafter `CRASH3`) extends the standard `CRASH` photo-ionisation algorithm to the treatment of the most cosmologically relevant metals in atomic form: C, O and Si. The current numerical scheme is based on a new pipeline which combines the excellent capabilities of `CRASH` in tracing the radiation field with the sophisticated features of the photo-ionisation software `Cloudy` (Ferland et al. 1998). The inclusion of a considerably large set of data imposed by the numerous metal ionisation states has required a substantial source code re-engineering that introduces a new memory management and a re-modelling of the photon packet-to-cell interaction. `CRASH3` is consequently more modular, optimized and easily integrable with other codes. In the following, we briefly review the basic ingredients of the `CRASH` algorithm that are required to understand the implementation of the new version, and we refer the reader to the original papers for more specific details.

A `CRASH` simulation is defined by assigning the initial conditions (ICs) on a regular three-dimensional cartesian grid of a given dimension (N_c^3 cells) and a physical box linear size of L_b, specifying:

• the number density of H (n_H) and He (n_{He}), the gas temperature (T) and the ionisation fractions ($x_{HII} =$ n_{HII}/n_H, $x_{HeII} = n_{HeII}/n_{He}$ and $x_{HeIII} = n_{HeIII}/n_{He}$) at the initial time t_0;

• the number of ionising point sources (N_s), their position in cartesian coordinates, luminosity (L_s in erg s^{-1}) and spectral energy distribution (SED, S_s in erg s^{-1} Hz^{-1}) assigned as an array whose element provide the relative intensity of the radiation in the correspondent frequency bin (see MCK09 for more details);

• the simulation duration t_f and a given set of intermediate times $t_j \in \{t_0, \ldots, t_f\}$ to store the values of the relevant physical quantities;

• the intensity and spectral energy distribution of a background radiation, if present.

The simulation run consists in emitting photon packets from the ionising sources and following their propagation through the domain. Each photon packet keeps traveling and depositing ionising photons in the crossed cells, as far as its content in photons is completely extinguished or it escapes from the simulated box (although periodic boundary conditions in the packets propagation are possible).

At each cell crossing, `CRASH` simulates the radiation-to-gas interaction by evaluating the absorption probability for a single photon packet as:

$$P(\tau) = 1 - e^{-\tau}, \tag{1}$$

where τ is the total gas optical depth of the cell given by the sum of the contributions from the different species, i.e. $\tau = \tau_{HI} + \tau_{HeI} + \tau_{HeII}$. The number of photons absorbed in the cell can then be estimated as:

$$N_\gamma \left(1 - e^{-\tau}\right), \tag{2}$$

where N_γ indicates the photon content of a packet entering the cell.

The number of the deposited photons for each spectral frequency is then used to compute the contribution of photo-ionisation and photo-heating to the evolution of x_{HII}, x_{HeII}, x_{HeIII} and T. The set of equations solved in the code is described in detail in Maselli et al. (2003) and in MCK09.

For the sake of the following discussion, we remind here that the evolution of the thermal state of the gas in each cell is regulated by the formula:

$$\frac{dT}{dt} = \frac{2}{3k_B p} \left[k_B T \frac{dp}{dt} + \mathcal{H}(T, x_i) - \Lambda(T, x_i) \right], \tag{3}$$

where p is the number of free particles per unit volume, $\mathcal{H}$ and Λ are respectively the heating and the cooling functions and the subscript i refers to all the ion species composing the gas. k_B is the Boltzmann constant. The heating function is determined by computing the photo-heating resulting from the photon-to-gas interaction discussed above, while Λ is calculated by adding up the contribution of various radiative processes: collisional ionisation and excitation, recombinations, Bremsstrahlung and Compton cooling. Differently from photo-heating, these processes are treated as continuous processes, described by their respective rates (see Maselli et al. 2003 for details).

3 CLOUDY

`Cloudy` (Ferland et al. 1998) is a code designed to simulate the physics of the photo-ionised regions produced by a wide

class of sources ranging from the high temperature blue stars to the strong X-ray emitting Active Galactic Nuclei. The main goal of `Cloudy` is the prediction of the physical state of photo-ionised clouds including all the observably accessible spectral lines. The latest stable release of `Cloudy` (at the time of writing v. 10.0[1]) simulates a gas which includes all the heavy elements of the typical solar composition and the contribution of dust grains and molecules present in the ISM.

In this Section we will focus on the description of the `Cloudy` features that have been primarily used to implement `CRASH3`. The reader interested in the details of the code implementation or in reviewing the many physical processes included can find more appropriate references in Ferland et al. (1998) and Ferland (2003).

Unlike `CRASH`, `Cloudy` is a 1D code assuming as preferred geometrical configuration a symmetrical gas distribution around a single emitting source, with photons propagating along the radial direction. `Cloudy` can also simulate the diffuse continuum re-emitted by recombining gas as nearly isotropic component under the assumption that the diffuse field contribution is generally small and can be treated by lower order approximations. Additional isotropic background fields can also be handled, as long as their shape and intensity are specified by the user. Some popular background models (like the Haardt and Madau cosmic UV spectrum described in Madau & Haardt 2009) are already distributed with the code. The contribution of the Cosmic Microwave Background (CMB) radiation can also be accounted for because it is an important source of Compton cooling for low density gas configurations typical of the IGM.

The micro-physics implemented in `Cloudy` is very accurate: it includes all the metals present in the typical solar composition (Grevesse and Sauval 1998) described as multi-level systems and treated self-consistently with the ions of the lightest 30 elements. Photo-ionisation from valence, inner shells and many excited states, as well as collisional ionisation by both thermal and supra-thermal electrons and charge transfer, are included as ionisation mechanisms. The gas recombination physics is simulated including the charge exchange, radiative recombination, and dielectronic recombination processes. `Cloudy` simulates all these processes adopting an approximation method for the radiation field evaluation known as escape probabilities method (Hubeny 2001), instead of evaluating the full radiative transfer as done by `CRASH`. This choice implies the loss of many details pertaining the line properties description, e.g. line pumping by the incident continuum, photon destruction by collisional deactivation and line overlap. In the standard release of `CRASH` the details of the lines are not accounted for and the above limitations are thus negligible.

Once the characteristics of the source and the species involved in the calculation are set up, `Cloudy` estimates the radial distribution of the ionisation and temperature fields by simultaneously solving the equations of ionisation and thermal equilibrium (Dopita & Sutherland 2003; Osterbrock & Ferland 2005). A static solution describing the physical state of the gas is then found by dividing the domain in smaller regions and iterating until convergence is reached. The usual assumption of such calculations is that

atomic processes occur on timescales much shorter than the temporal scales of the macro-physical system. `Cloudy` does not 'a priori' assume that the gas is in equilibrium and the solution provided is a general non-equilibrium ionisation configuration for a static medium that does not retain any information of the temporal evolution of the system towards the converging state. A large set of information about the relevance of the physical processes that establish the final convergence, and the details of the line emission processes are also provided with a great level of detail. This microphysic treatment can not be directly handled in `CRASH` with the same level of accuracy.

`Cloudy` describes the thermal equilibrium of the photo-ionised gas providing the local thermal balance obtained in each simulated sub-region. In the absence of non-thermal electrons produced by high-energy photons, this thermodynamic equilibrium is generally specified by the electron temperature T_e, because the electron velocity distribution of the gas is predominantly Maxwellian. Despite `CRASH` does not distinguish between the contribution of the different species to the gas temperature as calculated in eq. 3, in practice $T \sim T_e$ to a good approximation, and thus it is consistent with the output from `Cloudy`. It should be clarified though that `Cloudy` provides a gradient of temperatures within the simulated region. Because the `CRASH` resolution is a single cell, whenever we use a temperature provided by `Cloudy` this should be intended as the volume average over a cell. In the following we will always refer to the temperature as T.

Implementing `CRASH3` we have minimised the differences between the two codes, e.g. by disabling in `Cloudy` all the physical processes non explicitly treated in `CRASH` such as molecule and dust grain physics, charge transfer effects and radiation pressure, among others. In addition, while `CRASH` simulates the propagation of hydrogen ionising photons, `Cloudy` requires that any spectral information is provided in the energy range $13.6136 \cdot 10^{-8}$ eV$< E < 100$ MeV. For this reason, the spectrum used as input for `Cloudy` is the one provided by `CRASH` in the frequency range 13.6 eV$\leqslant E \leqslant E_{max}$ (see following Section), while it is set to zero for $13.6136 \cdot 10^{-8}$ eV$< E <$13.6 eV and $E_{max} < E <$100 MeV, where E_{max} is the energy corresponding to the higher frequency sampled in the `CRASH` simulation (see MCK09 for more details). The deeply different set-up of the simulations in `CRASH` and `Cloudy`, both in geometrical configuration and in the gas micro-physics, has made the building of the common pipeline a non trivial task. This will be detailed in the following Sections.

4   THE INCLUSION OF METALS IN CRASH

The extension of the `CRASH` algorithm with the full microphysics of metals is hardly viable because of the extreme complexity of the metal electronic structure which would increase the computational costs of a RT simulation to unacceptably high levels (see Dopita & Sutherland 2003; Draine 2011 and references therein for a modern introduction to the physics of the metals in ionised regions).

For this reason, we have adopted a hybrid approach in which `CRASH` performs the RT only through H and He, while the metal ionisation states are implemented self-consistently, but they are calculated with `Cloudy`. The two algorithms

---

[1] http://www.nublado.org

interact within a single pipeline called `CRASH3`, which is sketched in Figure 1. It should be noted that, if the radiative transfer is performed in a cosmological context, the pipeline applies to each single redshift, z. In this case, in addition to the ICs of the RT simulations, other physical quantities might depend on z, e.g. the cooling off the CMB radiation.

More specifically, `CRASH3` recognises the metal enriched sub-domain by applying a masking technique to it and by labelling the enriched cells, which are indicated here with the subscript m. After masking the m-cells containing metals, it derives the spectral energy distribution and luminosity of the ionising radiation present in each of the m-cells $(S, L)_m$, which are then used to query a dynamic database (DB) of configurations pre-computed with `Cloudy` to identify the corresponding ionisation states of the metals and the temperature of the gas. This procedure is repeated for a set of times $t_k \in \{t_0, \ldots, t_f\}$ and the physical state the enriched cells is then evaluated as a sequence of k_f equilibrium configurations at t_k. To ensure that the ionisation level of the metals is consistent with the energy configuration, the pipeline checks that the ionisation fractions of H and He evaluated by `Cloudy` and `CRASH` are in agreement. An example of this internal convergence test can be found in Section 5.1.1.

It should be noted that this approach neglects the contribution of metals to the optical depth, as well as to the diffuse radiation emitted by recombining gas. This approximation is justified as long as the metal abundances are very small compared to those of H and He. In fact, when the number density of heavy elements $n_Z \gtrsim 10^{-3} n_H$, the total photo-ionisation cross section starts to be dominated by the metal component (see Draine 2011, Chapter thirteen for a complete discussion). Because the metallicity observed in the IGM is typically below this value (see the Introduction), the above assumption is justified in the cases of our interest.

As detailed in Section 3, `Cloudy` can deal with either a single source configuration or a background radiation. If only a single source is present in the computational domain of `CRASH` or when each cell is illuminated from a preferential direction, then the `Cloudy` point source configuration should be used to estimate the ionisation and temperature state of the cell. When instead a cell is illuminated more or less uniformly from all directions, then the background radiation set-up should be adopted.

In the current implementation of `CRASH3` we have included the species C, O and Si, which are the most abundant metals observed in the IGM (see the Introduction). However, the inclusion of other species, which may be relevant for a more accurate estimate of the gas cooling function, is a straightforward extension of the present scheme (see Sec. 5.1.5).

Despite the conceptual simplicity of the approach described above, the coupling of `CRASH` and `Cloudy` in a single numerical scheme presents several technical challenges. In the following we will describe in more detail the strategy adopted for such integration and some aspects of the pipeline.

4.1 Step 1: initial conditions

The starting point of the pipeline is the set-up of the `CRASH3` ICs, which are the same of `CRASH` as specified in Section 2,
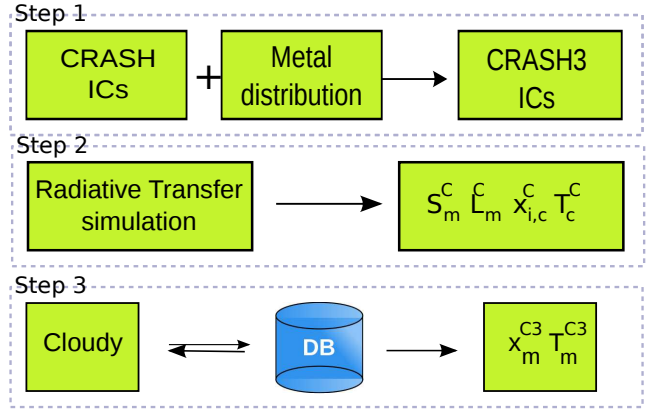

Figure 1. `CRASH3` simulation pipeline. The quantities S, L, x_i and T are the SED, luminosity, ionisation fractions (per species i) and gas temperature. The subscripts c and m refer to all the cells in the computational domain and the metal enriched cells only, while the superscripts ^{C} and ^{C3} refer respectively to the quantities provided by the radiative transfer simulation in Step 2 and by the database (DB), i.e. as a product of the full `CRASH3` pipeline. See text for more details.

with the addition of the spatial distribution and abundance of all the metal species present in the computational domain. These can be artificially created by hand or can be obtained as a result of e.g. hydrodynamic simulations that include physical prescriptions for metal production and spreading.

A preliminary analysis of the spatial distribution of metals allows to identify the m-cells that need to track the radiation field (Step 2) and then query the pre-computed DB (Step 3). To identify these cells a boolean mask is built isolating the enriched portion of the simulation volume. The building of the mask can be performed before the beginning of the simulation and passed as additional IC or can be created in memory during the simulation initialization. If the mask contains m-true values, a shadow map of m cell spectra, S_m^C, and luminosities, L_m^C, is allocated to store the shapes and luminosities of the incoming packets: each time a packet enters a cell, the mask is used to check whether the cell is an enriched one and consequently S_m^C and L_m^C should be updated (see Step 2). The masking has been designed to optimise the performances of the code, but in principle the SED and luminosity can be calculated in each cell of the computational domain, if required.

4.2 Step 2: radiative transfer simulation

The next step (Step 2 in Fig. 1) consists in performing a RT simulation which, in addition to the evaluation of $(x_i, T)_c^C$ in all the cells of the domain, tracks also the SED and luminosity of the ionising radiation in each of the m metal enriched cells $(S, L)_m^C$. All the above physical quantities are stored at times t_k, as already mentioned above. The values of $(S, L)_m^C$ at t_k are determined adding up the contribution of all the incoming photon packets up to that time. In practice, the code tracks all the multi-frequency packets entering the cell and calculates L_m^C as the sum of the luminosities of all the packets, while S_m^C as the average SED in each frequency bin.

4.3 Step 3: determination of the physical state of the metal enriched cells

Finally, a search engine[2] looks for the `Cloudy` precomputed configuration that best matches the values of H, He, metal number densities and $(x_{\mathrm{HII}}, x_{\mathrm{HeII}}, x_{\mathrm{HeIII}}, S, L)_m^C(t_k)$. The best fitting configuration then provides the ionisation fractions of the metal ions and the temperatures T_m^{C3} of the gas in the metal enriched sub-domain (Step 3 in Fig. 1).

If the matching criteria are not satisfied (see below for more details), the database is extended with additional on-the-fly `Cloudy` runs. It is important to point out that Step 3 does not severely affect the basic algorithm performances because it is confined only to the m enriched cells and a large number of `Cloudy` calculations are pre-computed and stored in the DB.

A correct computation of the temperature is not trivial, because also in the absence of metals the temperatures predicted by `CRASH` and `Cloudy` are not in perfect agreement in the vicinity of the point sources (MCK09). More generally, it has been shown that different approaches to the radiative transfer do not always predict consistent temperatures in such regions (Iliev et al. 2006b). This means that every time a discrepancy between T_m^C and T_m^{C3} occurs it is important to understand if this is due to the presence of metals or just to the differences in the two codes. For these reasons we allow some flexibility in the matching criteria for the temperature and we define a temperature deviation ΔT_m^i as:

$$\Delta T_m^i = T_m^C - T_m^{C3}, \qquad (4)$$

where $i = met$ refers to the deviation calculated for a gas contaminated by metals, while $i = pris$ refers to a pristine gas. The difference $\Delta T_m = \Delta T_m^{met} - \Delta T_m^{pris}$ is $\geqslant 0$ by design and it is due only to the effect of metals. In the enriched cells in which ΔT_m is greater than some threshold value for the maximum tolerated deviation, T_m^C is replaced by T_m^{C3}. We apply this correction (accounting for the metals feedback on the temperatures) when the ΔT_m is higher than $\sim$10% T_m^{C3} without metals. However the value adopted for the threshold depends on the physical problem being study and for this reason the criteria for the threshold can be defined at the beginning of each simulation. Note that the temperature correction has some weak feedback on the physical state of the gas also via its recombination coefficients, especially for the helium component.

In realistic applications, the temperature provided by the hydrodynamics (T_{hydro}) could be significantly higher than the temperature established by the RT. This generally happens in gas shocked regions where the metal ions are determined mainly by collisional ionisation rather than photo-ionisation. Collisional ionisation is correctly handled by the pipeline at Step 2 for H and He, because `CRASH` selects $T = max(T^C, T_{hydro})$ during its simulation initialisation process, maintaining the right temperature. Note that these regions are known as ICs, and a masking technique can be used to isolate them from the standard pipeline workflow. The ionisation status of the metal component eventually present in these cells can be determined from `Cloudy`

[2] We have implemented a Standard Query Language database using one of the codes freely available to the scientific community.

pre-computed tables, and by interpolating the gas number density, metallicity, temperature, as well as the ionisation fractions of hydrogen and helium. For more details on this technique see Oppenheimer & Davé (2006) and references therein.

5 TESTS

In this Section we present three tests designed to establish the reliability of the new code. The first test (Section 5.1) concentrates on the standard Strömgren sphere case, albeit of a metal enriched gas. The second test (Section 5.2) investigates the sensitivity of `CRASH3` to fluctuations of the radiation field induced by different source types and tracked by the many metal ionisation states. Finally, the third test (Section 5.3) describes a more realistic physical configuration by using as ICs those from a snapshot of a hydrodynamic simulation.

Hereafter the gas metallicity (or equivalently the metal mass fraction) is defined as $Z_g = M_Z/M_g$, where M_Z is the total mass of the elements with atomic number higher than 2 and M_g is the total mass of the gas; the metal mass fraction in the Sun is set to $Z_\odot \approx 0.0126$, according to the metal abundances relative to hydrogen as reported in the `Cloudy` Hazy guide I and references therein, and taking into account the 10 most abundant elements: H, He, C, N, O, Ne, Si, Mg, S and Fe.

Unless otherwise stated, the metal feedback on the calculation of the gas temperature is neglected and we use $k_f = 100$.

5.1 Test 1: Strömgren sphere with metals

We consider a configuration similar to the one in Test 2 of the Cosmological Radiative Transfer Comparison Project (Iliev et al. 2006a), but for the presence of metals.

The simulation box has a co-moving side length of 6.6 kpc and it is mapped onto a regular grid of $N_c^3 = 128^3$ cells. The gas is assumed to be uniform and neutral at the initial temperature $T = 100$ K, with a number density $n_{gas} = 0.1$ cm^{-3} and a hydrogen (helium) number fraction of 0.9 (0.1). Only one point source is considered with coordinates (1,1,1), a black-body spectrum at temperature $T = 10^5$ K and ionisation rate of $\dot{N} = 10^{51}$ phot s^{-1} (i.e. a luminosity $L \simeq 5 \cdot 10^{40}$ erg s^{-1}). To ensure a good convergence of the MC scheme, the source radiation field has been sampled by $2 \cdot 10^8$ photon packets. The redshift of the simulation is set at $z = 0$ and the simulation duration at $t_f = 5 \cdot 10^8$ yrs, i.e. several times the recombination time characteristic of the simulated gas configuration. This choice assures that convergence is reached at the end of the simulation. We uniformly contaminate the gas with carbon ($n_C \simeq 2.2 \cdot 10^{-7}$ cm^{-3}), oxygen ($n_O \simeq 4.41 \cdot 10^{-7}$ cm^{-3}) and silicon ($n_{Si} \simeq 3.12 \cdot 10^{-8}$ cm^{-3}), corresponding to $Z_g = 6.45 \cdot 10^{-3} Z_\odot$. These numbers are obtained maintaining the metal abundances relative to hydrogen mentioned above. Finally, the source spectrum is sampled by 91 frequencies and it extends to an energy $E_{max} = 0.2$ keV, in order to include the photo-ionisation edge of the ion O VI.

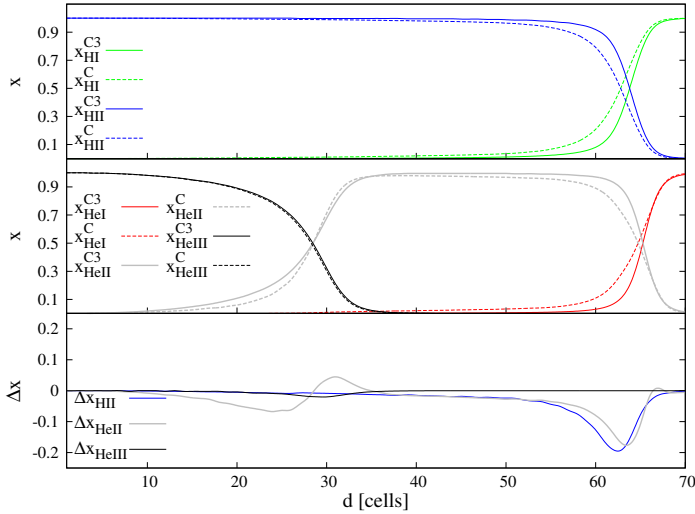Although we contaminate the entire box with metals, it is possible to significantly reduce the number of DB queries

Figure 2. Convergence between Step 2 (dashed lines and variables with superscript ^{C}) and Step 3 (solid lines and variables with superscript ^{C3}) for Test 1 in the absence of metals (see text for details). The lines refer to the simulation time $t_f = 5 \cdot 10^8$ yrs. At distances larger than 70 cells the gas is neutral and therefore it is not shown in the plots. **Top panel:** profile of x_{HI} (green lines) and x_{HII} (blue). **Middle panel:** same as above for x_{HeI} (red lines), x_{HeII} (gray) and x_{HeIII} (black). **Bottom panel:** $\Delta x_i = x_i^C - x_i^{C3}$ for i=H II (blue line), He II (gray) and He III (black).
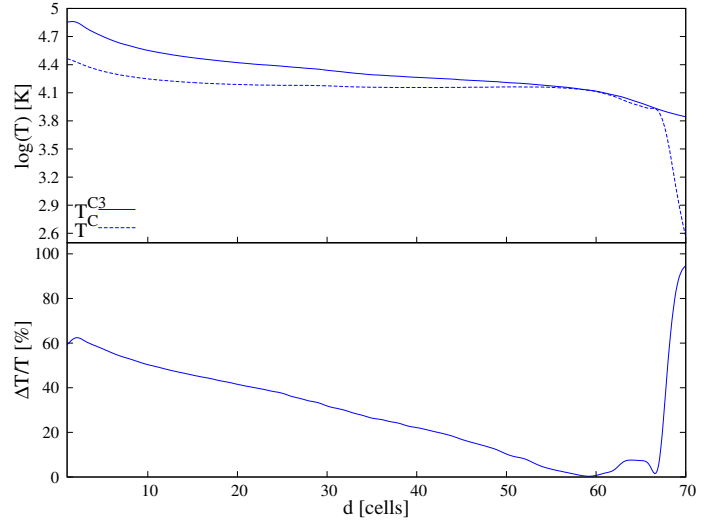
Figure 3. Top panel: Temperature convergence between Step 2 (T^C, dashed line) and Step 3 (T^{C3}, solid line) for Test 1 in the absence of metals (see text for details). The lines refer to the simulation time $t_f = 5 \cdot 10^8$ yrs. **Bottom panel:** relative difference $\Delta T / T = (T^{C3} - T^C)/T^{C3}$.

taking advantage of the spherical geometry of the problem and assuming that each radial direction is equivalent. This is justified as long as the number of photon packets used is large enough that the fluctuations induced by the Monte Carlo sampling are negligible. We then apply a spherical average of all the relevant physical quantities at each distance d (expressed in cell unit) from the ionising source, and we use these averaged values to search for the better-matching configuration in the DB. All the quantities discussed and displayed in this Test should be intended as explained above, i.e. as spherically averaged values.

5.1.1 Pipeline convergence

Before proceeding further with the analysis of the results, we discuss the internal convergence of the pipeline. More specifically, we need to assure that the ionisation fractions x_{HII}, x_{HeII} and x_{HeIII} calculated in Step 2 and Step 3 of the pipeline are in agreement with some user-defined threshold. The same needs to be true for the temperature T if the effect of metals is negligible. This would ensure that the physical configuration and energetic balance evaluated in Steps 2 and 3 are fully consistent. To this aim we run Test 1 in the absence of heavy elements.

In Figure 2 we show the profile of x_{HI}, x_{HII} (top panel), x_{HeI}, x_{HeII} and x_{HeIII} (middle panel) as evaluated by Step 2 (dashed lines and variables with superscript ^{C}) and Step 3 (solid lines and variables with superscript ^{C3}) at the time $t_f = 5 \cdot 10^8$yrs. The values of x_{HI} and x_{HII} result in agreement within 10^{-4} for $d < 40$ cells (~ 2 kpc) and within 10^{-2} up to the ionisation front (I-front), identified as the location

where the ionised fraction drops below ~ 0.8. The agreement degrades to ~ 18 % (with respect to the maximum absolute difference between ionisation fractions) in the two cells in which the curves of x_{HI} and x_{HII} cross, and then it restores up to 10^{-3}. Both codes predict the crossing in the same cell. A similar behaviour is shown in the middle panel for helium. A discrepancy of ~ 7 % in the x_{HeII} curves is seen at a distance $d \sim 22$ cells, when the abundance of He II starts to increase. He III results in an even better agreement, up to 10^{-4}. Reasonable accuracy (less than 20 %) is also reached in the fronts of He II and He I where both algorithms predict a similar shape. Because at the end of the HII region the intensity of the radiation has dropped substantially (see following Section), sometimes `Cloudy` does not find a convergent solution in few iterations, and this results in a poorer agreement between Step 2 and 3.

The above differences are more evident in the bottom panel of the Figure, where we show the absolute difference $\Delta x_i = x_i^C - x_i^{C3}$ for i=H II, He II and He III.

Despite the satisfying agreement in the `CRASH3` implementation, some small discrepancies remain due to the differences between the `CRASH` and `Cloudy` geometries and the numerical implementation of the ionisation and energy equations (see Sec. 3). We found that a critical ingredient to reach an acceptable convergence is to sample the source spectrum with a large number of frequency bins (see details in the Test Section). This is necessary because the helium component is very sensitive to this sampling, in particular in the vicinity of the ionisation potential of He II.

The temperature radial profiles estimated in the two Steps are shown in Figure 3 (top panel). The curves present large discrepancies in the cells near the source, with a relative variation $\Delta T / T = (T^{C3} - T^C)/T^{C3}$ as high as 60 percent. The difference drops below 30 percent for $d > 30$ cells. This is not reflected in the H and He profiles shown in Figure 2 because of the weak temperature dependence
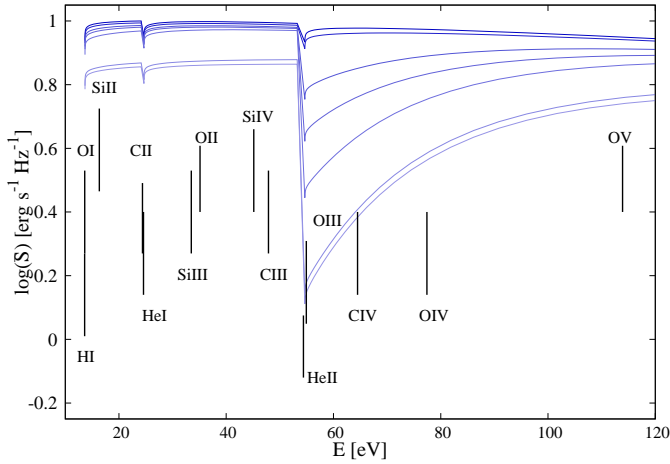
Figure 4. Normalized logarithm of the spherically averaged spectra. Lines refer to the spectra at a distance d (from the top to the bottom) of 20, 27, 38, 45, 55, 69 and 70 cells. The spectra correspond to a time $t_f = 5 \cdot 10^8$ yrs. As a reference, some ionisation potentials are also indicated as vertical lines.

in the gas recombination coefficients. Such a difference has been already noticed and discussed in the `CRASH` vs `Cloudy` comparison test in MCK09 and can be ascribed just to the different implementation of the temperature estimate in the two codes.

Because `CRASH` updates the temperature (compared to its initial value) only in those cells reached by ionising photons, outside the HII region T drops to the initial value of 100 K. On the other hand, the temperature calculated by Step 3 is provided by `Cloudy` and, as already mentioned above, all the regions where the intensity of the radiation is too faint do not provide a convergent solution. In the few cells in which `Cloudy` cannot provide a reliable estimate because of the too weak radiation field, the `CRASH` temperature T^C is retained as better estimate of the physical temperature at the front.

These convergence tests have been repeated using different ICs for the gas number density and the source luminosity. More specifically, we have run simulations on a grid of cases with values $n_{gas} = 1, 0.1, 0.01 \, \text{cm}^{-3}$ and $\dot{N} = 5 \cdot 10^{50}, 5 \cdot 10^{51} \text{phot s}^{-1}$. It is found that, as the gas density decreases, the agreement improves for the H species, while small discrepancies still remaining in the He species. Such discrepancies are, on the other hand, always below 20 % and remain limited to the small number of cells encompassing the ionisation fronts. A similar improvement is observed also for the gas temperature convergence.

Hereafter all the variables will refer to values calculated at Step 3 and the superscript ^{C3} will be omitted to simplify the notation.

5.1.2 Ionisation field

In Figure 4 we show how the spectral shape of the ionising radiation field described in terms of its spherical average

E_{ion} [eV]	H	He	C	O	Si
E_{xI}	13.598	24.587	11.260	13.618	8.152
E_{xII}		54.400	24.383	35.118	16.346
E_{xIII}			47.888	54.936	33.493
E_{xIV}			64.494	77.414	45.142
E_{xV}			392.090	113.900	166.770
E_{xVI}			489.997	138.121	205.060

Table 1. Ionisation potentials for H, He, C, O and Si up to the ionisation level VI as used in `Cloudy`.
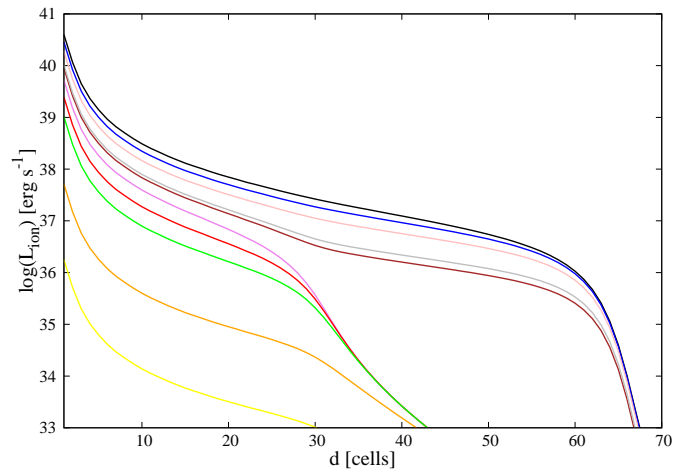

Figure 5. Logarithm of the photo-ionising luminosity, L_{ion}, as function of d at a time $t_f = 5 \cdot 10^8$ yrs. Different curves are calculated integrating all the photons above the ionisation threshold of (from the top to the bottom curve): H I (black line), He I (blue), Si III (pink), Si IV (gray), C III (brown), He II (violet), C IV (red), O IV (green), O V (orange), O VI (yellow).

(obtained as described at the beginning of Sec. 5) changes with the distance d as a result of geometrical dilution and filtering. Each line refers to the simulation time $t_f = 5 \cdot 10^8$ yrs.

The spectra shown are truncated at $E = 120$ eV to have a better visualisation of the most relevant line potentials. The upper curve corresponds to a distance of $d = 20$ cells, while the lower to $d = 70$ cells; at larger distances the intensity of the radiation becomes too faint to solve the ionisation equilibrium in every configuration at Step 3 of the `CRASH3` pipeline. Because the medium is fully transparent in H and He up to a distance $d = 20$ cells, we have normalized the spectra in the Figure to the maximum value of the spectrum at $d = 20$ cells. This choice allows a better visualisation of the shaping effects by the partially ionised regions. The ionisation potentials of the metals enriching the box (see Table 1) are also shown as reference even if, by design, metals do not contribute to the filtering of the ionising radiation. The absorption due to H I, He I and He II is clearly visible in correspondence of the respective ionisation potential, i.e. 13.6 eV, 24.6 eV and 54.4 eV.
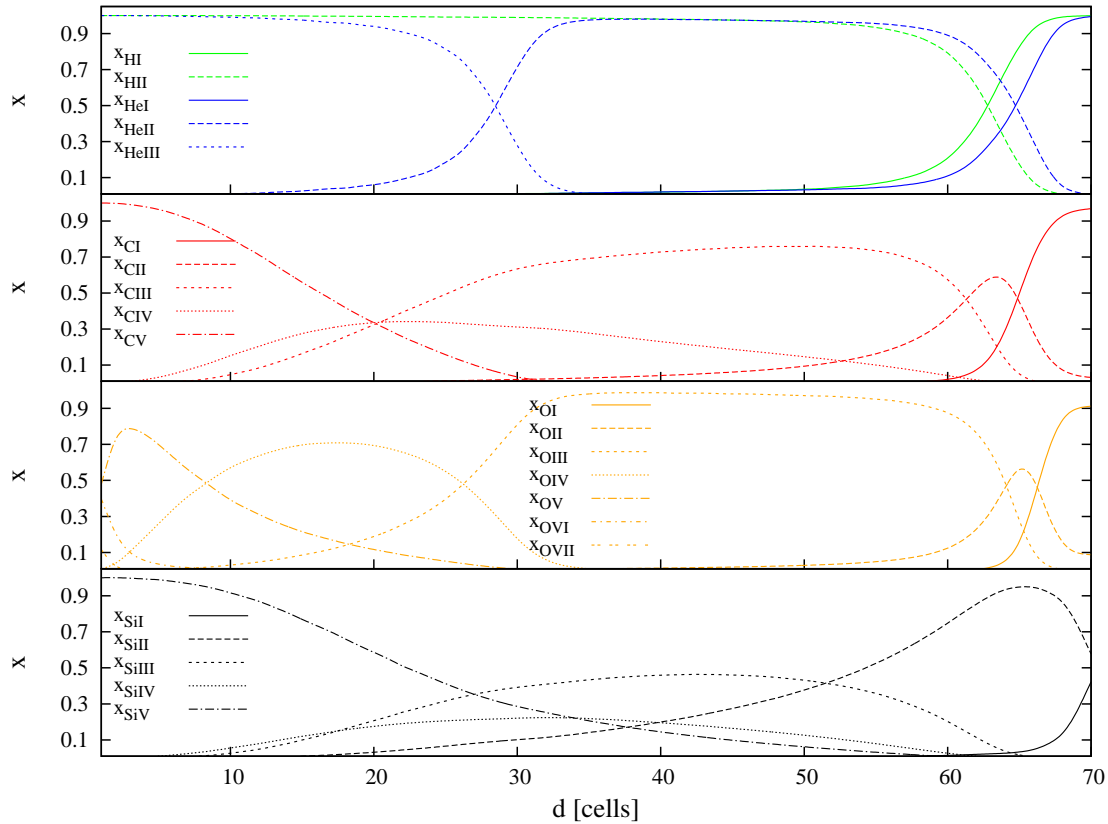
Figure 6. Fractions of the various components as a function of distance d from the source in Test 1. The values are taken at the simulation time $t_f = 5 \cdot 10^8$ yrs. From the top panel to the bottom the species are: H (green lines) and He (blue); C (red); O (orange); and Si (black). In each panel the same ionisation states are represented by the same line-styles: solid lines refer to the neutral components (e.g. O I), long dashed to the first ionisation state (e.g. O II), short dashed to the second (e.g. O III), dotted to the third (e.g. O IV), long dashed-dotted to the fourth (e.g. O V), short dashed-dotted to O VI, and dashed-spaced to O VII.

Figure 5 shows the total photo-ionising luminosity, L_{ion}, available for ionisation of some reference species as a function of d at a time $t_f = 5 \cdot 10^8$ yrs. L_{ion} is defined as:

$$L_{ion}(d) = h_p^{-1} \int_{E_{ion}}^{E_{max}} S(E, d) \, dE, \qquad (5)$$

where E_{ion} is the ionisation potential of the species considered (see Table 1 for reference) and h_p is the Planck constant.

Because the spectrum includes only photons with $E > 13.6$ eV, L_{ion} is an underestimate for those elements with an ionisation potential below 13.6 eV, i.e. carbon and silicon. Note that L_{OI}, L_{CII} and L_{OIII} overlap respectively with L_{HI} (black line), L_{HeI} (blue) and L_{HeII} (violet) because of the very similar ionisation potential. If we increased the frequency resolution of the spectrum the curves would show some small difference. This would be at the expense of the computational time without significant advantages in the accuracy of the metal ionisation state. For this reason we do not further increase the frequency resolution. Notice that all the luminosities decrease smoothly with d; this is consistent with the behaviour expected in an HII region, as already reported and extensively commented in Maselli et al. (2003) and MCK09 for the hydrogen and helium components.

5.1.3 Metal ionisation states

We now analyse the behaviour of the metal ionisation states, plotted in Figure 6. Before discussing the details of the Figure, it is necessary to point out that the balance among the different ions is primarily established by the relative values of their ionisation potentials and of their recombination coefficients (see Ferland 2003). It also depends on the spectral distribution of the radiation field and its variations with the distance from the source, as induced by the radiative transfer effects. The complex interplay between these numerous processes makes the interpretation of the results non trivial; despite this, some trends have a straightforward explanation.

Because of the small amount of metals included in this test, we expect their impact on the evolution of H and He to be negligible. This is confirmed by a comparison of the curves in the top panel of the Figure to the corresponding curves in Figure 2, which are obtained without metals. The maximum difference is ~ 7 % across the I-front of H II. Additional effects on the ionisation fractions induced by an increase in the gas metallicity will be investigated in Section 5.1.5.

We now turn to analyse the behaviour of carbon (second panel from the top). For $d < 30$ cells, C is in the form of C III, C IV and C V, with a predominance of the latter close to the source. This high ionisation level is obtained from
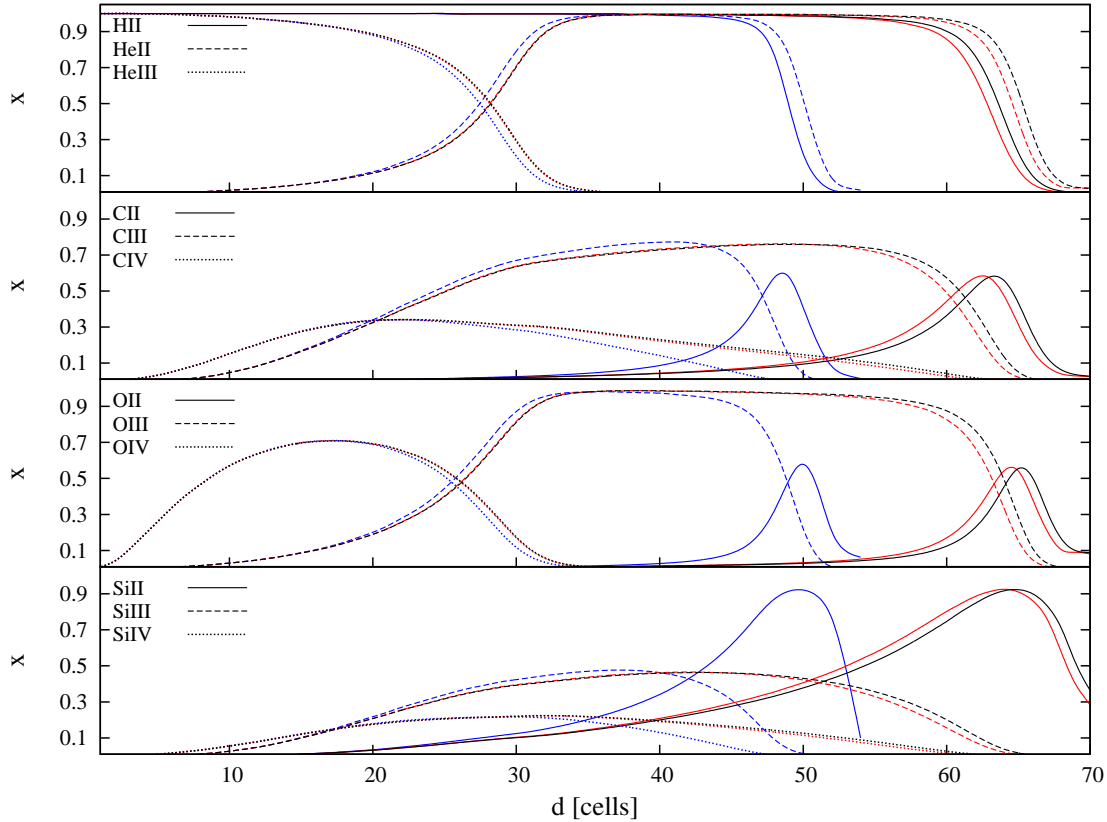
Figure 7. Fractions of the various components as a function of the distance d from the source in Test 1. From the top panel to the bottom the species are: H and He; C; O; and Si. In each panel colors refer to different simulation time: $t = 10^6$ (blue), 10^7 (red) and $5 \cdot 10^8$ yrs (black).

a combination of collisional ionisation and photo-ionisation. The evolution of C III is very similar to that of He II because of the similar ionisation potentials (see Fig. 4). The abundance of C IV is dictated by the evolution of C III and C V, and their relative recombination coefficients. C IV is present throughout the entire HII region, with x_{CIV} being always below 30 percent. For $d \gtrsim 30$ cells x_{CV} goes to zero because only few C IV ionising photons are available (see Fig. 5 as a reference). The ionisation potential of C V is outside our frequency range (see Table 1) and thus higher ionisation states are not present. Because of the paucity of photons with $E > E_{\mathrm{CIII}}$, at $d > 30$ cells only C III is present in large quantities with $x_{\mathrm{CIII}} \sim 70\%$. At $d \sim 60$ cells, similarly to what happens to H II and He II, also C III declines and C II dominates. Finally, outside the HII region, only C I is present.

In the third panel from the top the ions of the oxygen are shown. The ionisation potential for O VI is the highest photo-ionising energy available in the adopted spectrum. A very small fraction of O VII is in fact present in few cells around the source. It should be noticed that collisional ionisation contributes to this fraction for $\sim 10\%$ at $T \geqslant 7 \cdot 10^4$ K, which is present when $d < 3$ cells. The presence of O VI, is more evident but it is consistently limited to the inner region of the ionised sphere and decreases rapidly with the distance from the source in favour of lower ionisation levels. For $d \gtrsim 30$ cells O III dominates the ionisation balance until it drops in favour of O II, roughly at the end of the HII

region. As for the other species, outside the HII region only O I is present.

In the bottom panel the behaviour of silicon is reported. Si V completely dominates the inner region of the Strömgren sphere, with a long tail extending to $d \sim 55$ cells, where it is in equilibrium with lower ionisation states. In the central region many ions are in equilibrium with a low ionisation fraction. Si III reaches a maximum fraction of ~ 0.4 at the center of the HII region. Si II dominates at $d > 52$ cells. The abundance of Si I in the outskirts of the HII region is much lower than the one of e.g. C I because of the lower number density of Si and the much larger cross section of Si I at the resonance (see Fig. 13.2 of Draine 2011).

In general, it is possible to say that in the vicinity of the source the most abundant species are those with the higher ionisation state compatible with the maximum potential in the spectrum, i.e. H II, He III, C V, O V and Si V. Despite E_{OV}, E_{OVI} and E_{SiV} being covered by the spectrum, the abundance of photons at these energies is so low that x_{OVI}, x_{OVII} and x_{SiVI} are negligible. As the distance increases, the luminosity available for ionisation decreases, in particular for ions with high ionisation potentials (see Fig. 5). This is reflected by the decrease of the abundance of these highly ionisation states and the predominance of lower ionisation states (e.g. He II, C III, O III and Si III). Species like Si IV and C IV are always present, although they are not dominant, because the spectrum of the ionising radiation maintains energies higher than E_{SiIII} and E_{CIII} throughout the HII region (see Fig. 5).
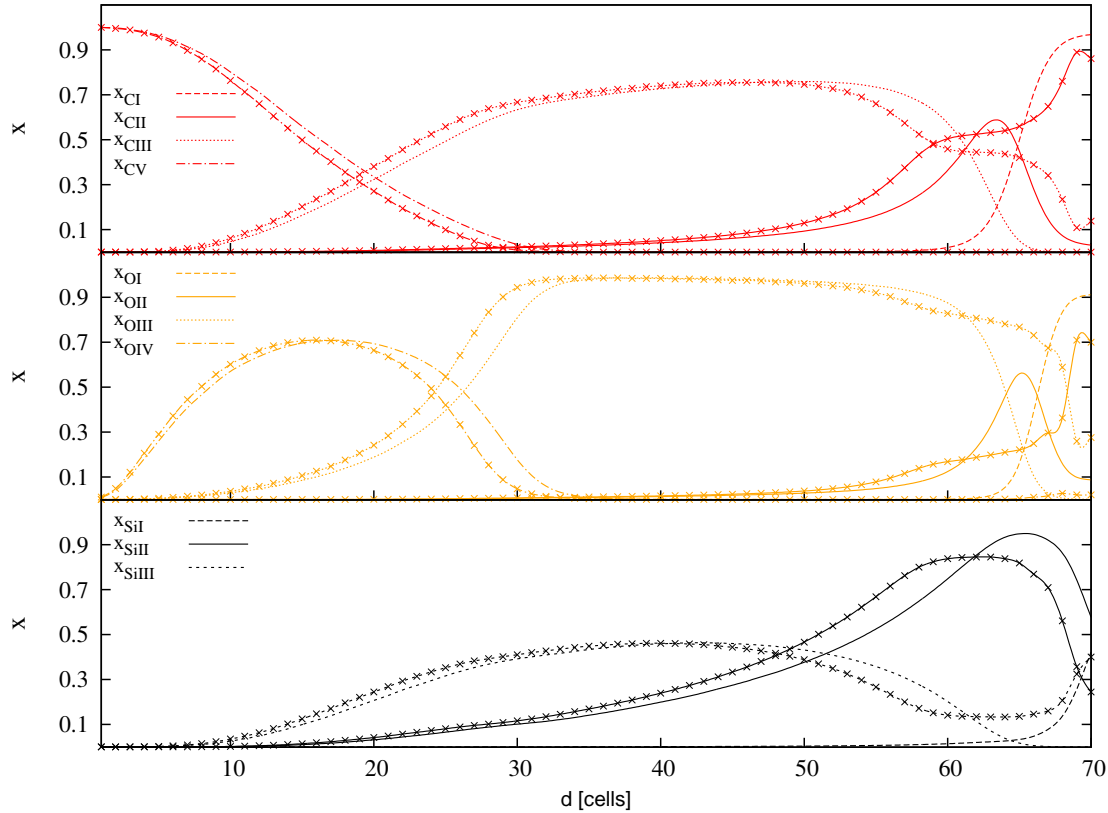
Figure 8. Fractions of C (**upper panel**), O (**middle**) and Si (**lower**) ions as a function of the distance d from the source in Test 1. In each panel, lines with crosses refer to Test 1 with the source spectrum extending to a lower ionising energy of E_{SiI}, rather than E_{HI}. Note that the neutral fractions in the former case are equal to zero in the range of cells shown here.

At even larger distances ($d > 60$ cells) the dominant species are typically singly ionised metals and the neutral components, due to the absence of ionizing radiation.

While the discussion above refers to the final gas configuration, in Figure 7 we show some reference species at different simulation times, i.e. $t = 10^6$, 10^7 and $5 \cdot 10^8$ yrs. It should be kept in mind that in this case no metal feedback is included in the calculation (see Sec. 5.1.5) and thus the profiles of the metal species at each time are independent from each other. While the shape of each species changes substantially between 10^6 and 10^7 yrs, for $t \gtrsim 10^7$ yrs they have almost converged. This is especially true for the metal ionisation potentials larger than the third and for He III. Overall, the comments made for Figure 6 at $t_f = 5 \cdot 10^8$ yrs apply also at earlier times.

5.1.4 *Effect of photons with $E < 13.6$ eV*

In this Section we discuss the impact of photons with $E < 13.6$ eV in the evaluation of metal ionisation states. Because the ionisation potential of C I and Si I is below E_{HI}, i.e. in a range which is not covered by **CRASH** and where the spectrum is set by default to zero, this means that photo-ionisation by photons with $E < 13.6$ eV is neglected, resulting in a systematic underestimate of x_{CII} and x_{SiII} as visible in the outer region of the Strömgren sphere.

To investigate this limitation of our pipeline, we have extended the spectrum to a lower energy of $E_{\mathrm{SiI}} = 8.152$ eV.

It should be kept in mind, though, that in the range E_{SiI}-E_{HI} the luminosity of the spectrum is overestimated because the absorption by metals (the only species contributing to the optical depth in this energy range) is not accounted for. This means that the change in the spectrum at these frequencies is due only to geometrical dilution. The approximation is more severe beyond the He II front (see Figure 6), where the only surviving radiation has energy below E_{HI} and the optical depth of the medium is dominated by the metals[3].

In Figure 8 we summarise the results of this run by showing the evolution of different C, O and Si ions. Lines with crosses refer to the case in which the source spectrum extends below 13.6 eV. In the inner part of the HII region the agreement between the curves with and without the inclusion of the low energy tail is excellent for the neutral fractions and the first ionisation state, while it gets worse for higher ionisation states. The reason is that, when the spectrum is extended below 13.6 eV additional physical processes become relevant, in particular line emission from collisional excitation. The most prominent case is the collisional excitation of the O IV line. While the behaviour of x_{OV} is the same in both cases (and for this reason it is not reported here), in the presence of non H I-ionising radiation O IV re-

---

[3] In realistic configurations other absorbers like dust and molecules could play a dominant role in establishing the optical depth of the medium at these frequencies, but these are not accounted for in **CRASH3**.

combines more quickly to O III, inducing the discrepancies observed between ~ 20-35 cells. Something similar happens to C V and C III, while C IV is not affected because it is not a dominant species at these distances, as shown in Figure 6. For the Si the differences are smaller. The picture in the outskirts of the HII region instead changes completely: not only do x_{CII}, x_{OII} and x_{SiII} extend outside the HII region, while the corresponding neutral components disappear, but also the higher ionisation states are affected. This results from a combination of the photo-ionisation due to the photons with energies below 13.6 eV and the additional physical processes mentioned above. At these distances the former effect has a larger impact than in the vicinity of the source, where ionisation is dominated by photons with energies above 13.6 eV. It should be noted that outside the HII regions, or, more correctly, when the absorption of photons is not dominated any more by H and He, our assumption of neglecting the metal contribution to the optical depth fails and the metal ionisation states are not calculated correctly any more[4].

5.1.5   Feedback by metals

In this Section we investigate the effect of metals on the evaluation of the gas temperature. In the Appendix the convergence of this feedback with respect to the choice of k_f is investigated. This is done by calculating T at the time $t_f = 5 \cdot 10^8$ yrs in the standard configuration of Test 1 and then changing the metallicity of the gas.

Test 1 has been repeated changing the gas metallicity Z_g, while maintaining the relative abundance of C, O and Si. In the upper panel of Figure 9 we show the results in terms of:

$$\Delta T/T \equiv \frac{T(0) - T(Z_g)}{T(0)}, \qquad (6)$$

where $T(0)$ is the value of the temperature relative to a configuration with $Z_g = 0$. The reference case ($Z_g = 0.0064 Z_\odot$, dashed line) does not show any significant metal cooling, with the exception of the region near to the source ($d < 5$ cells) where recombination and re-emission of high ionisation states of C, O and Si is more significant, inducing an average $\Delta T/T \sim 10\%$. Temperature deviations at the He II I-front ($d > 65$ cells), where the ionising radiation is very faint, are also present, with $\Delta T/T < 10\%$. Increasing the metallicity to one percent solar (solid line) does not change the results. Only at $Z_g = 0.064 Z_\odot$ (dashed-dotted line) some cooling is visible at each distance. In few cells near the source $\Delta T/T$ is as high as 40%, while it remains below 10 percent at $d > 10$ cells. The effect of metal cooling starts to be very significant for $Z_g \geqslant 0.64 Z_\odot$ (dashed-spaced line), with a $\Delta T/T \sim 60\%$ in the inner part of the HII region and ~ 15-20% also in its outer part.

Even if it is not shown in Figure 9, we have computed the solar and super-solar cases ($Z_g \geqslant 1 Z_\odot$), finding a deviation of $\Delta T/T > 50\%$ in the inner region, and values exceeding 40 percent up to $d \sim 45$ cells. These results confirm
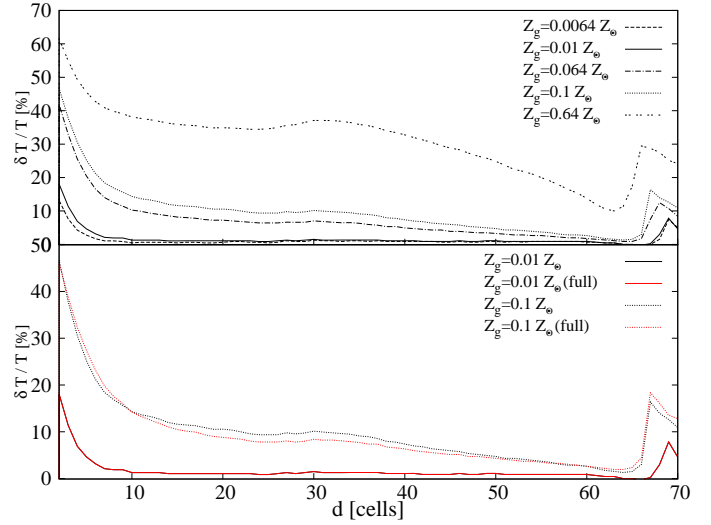
---

[4] Other important processes playing a relevant role in the outskirts of the HII region, as e.g. $O^+ + H \longleftrightarrow O + H^+$, have been deactivated in `Cloudy` by disabling the charge transfer. More references on the subject can be found in Draine (2011).

Figure 9. $\Delta T/T = (T(0) - T(Z_g))/T(0)$ as function of the distance d from the source in Test 1 at the simulation time $t_f = 5 \cdot 10^8$ yrs (see text for more details). **Upper panel:** the curves refer to a gas enriched by C, O and Si, and a metallicity Z_g of: $0.0064 Z_\odot$ (dashed line, reference value), $0.01 Z_\odot$ (solid), $0.064 Z_\odot$ (dashed-dotted), $0.1 Z_\odot$ (dotted) and $0.64 Z_\odot$ (dashed-spaced). **Lower panel:** the curves refer to a gas enriched only with C, O and Si (black lines) or with the ten most abundant elements in the solar composition (red). For both cases the gas metallicity Z_g is $0.01 Z_\odot$ (solid lines) and $0.1 Z_\odot$ (dotted).
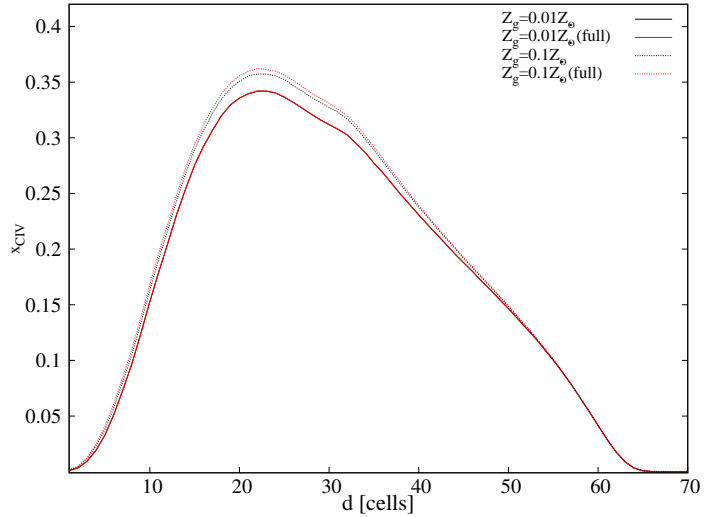

Figure 10. Fraction of C IV as function of the distance d from the source in Test 1 at the simulation time $t_f = 5 \cdot 10^8$ yrs. The curves refer to a gas enriched only with C, O and Si (black lines) or with the ten most abundant elements in the solar composition (red). For both cases the gas metallicity Z_g is $0.01 Z_\odot$ (solid lines) and $0.1 Z_\odot$ (dotted).

the dominant role played by the metal cooling in this metallicity range. These cases though should be considered only as indicative because in this metallicity regime the metal contribution to the absorption cannot be neglected and the assumptions of our method fail.

As a second step we have investigated the dependence of our results on the gas composition; this is shown in the bottom panel of Figure 9. More specifically, while the black lines
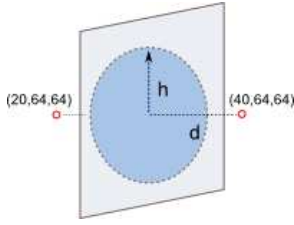
Figure 11. Sketch of the geometrical set-up used for Test 2.

are the equivalent of the ones in the upper panel, the red lines have been obtained including the 10 most abundant elements in the solar composition. Note that the red and black lines are not distinguishable in the reference metallicity case. In both cases the number densities of metals are such that their abundance relative to H is the same as those in the solar composition. It is clear that, at a fixed metallicity, the contribution of C, O and Si to the cooling is dominant compared to other elements, such as N, Ne, Mg, S and Fe. We have thus neglected such elements in all further tests. It should be noted that just adding the contribution of N, Ne, Mg, S and Fe to the gas metallicity (without keeping it constant) would bring Z_g from e.g. $0.0064 Z_\odot$ to $0.01 Z_\odot$, and $0.064 Z_\odot$ to $0.1 Z_\odot$.

In Figure 10 we finally report the effect of a varying metallicity and chemical composition on the ionisation fraction of C IV. It is clear that it is safe to neglect metals other than C, O and Si as their impact on the global ionisation equilibrium is limited at a maximum of few percent for $Z_g \gtrsim 0.1 Z_\odot$, while it is close to zero for lower metallicity. A similar effect is observed for all the other relevant ions. On the other hand, the dependence on the gas metallicity Z_g is higher and it changes for the various species. In some cases, like the one shown in the Figure (as well as e.g. O III and Si IV), the ionisation fraction of the species increases with increasing metallicity, while in others (as e.g. C III, O V and Si IV) the trend is reversed. It is beyond the scope of this paper though to discuss this issue in more details.

5.2 Test 2: metal fluctuations in the overlap of two HII regions

Here we study the behaviour of metals in the HII region overlap produced by two point sources located in cells $(20, 64, 64)$ and $(40, 64, 64)$. This geometrical set-up is sketched in Figure 11 and it is designed to investigate the sensitivity of our method to small changes in the source characteristics. This is done by varying the source ionising rates, $\dot{N}_1$ and $\dot{N}_2$, and their associated black-body spectral temperatures, T_1 and T_2. All the other numbers are the same as those in Test 1, with the exception of the gas number density which is $n_{gas} = 1$ cm^{-3}, to obtain a sharper overlap profile. Because in this test we are interested in studying the behaviour of metals only in the overlap region, we concentrate on the plane corresponding to $x = 30$ (blue circle in Fig. 11).

5.2.1 Reference case

We first describe the set-up used as reference case, with two identical sources with $\dot{N}_1 = \dot{N}_2 = 9 \cdot 10^{51}$ phot s^{-1} and $T_1 = T_2 = 10^5$ K. Similarly to Test 1, here we show the results
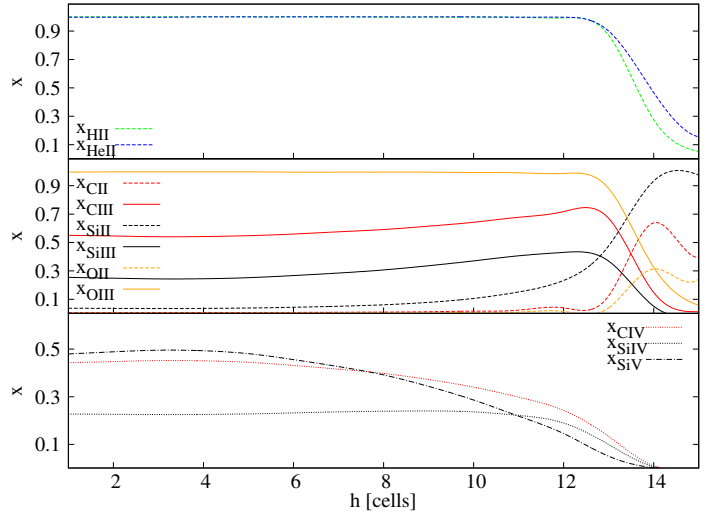

Figure 12. Ionisation fractions as function of h, evaluated in the plane equidistant from the two sources ($x = 30$) of Test 2 in the reference case. From top to bottom the panels refer to: $x_{\rm HII}$ (green dashed) and $x_{\rm HeII}$ (blue dashed); $x_{\rm CII}$ (red dashed), $x_{\rm CIII}$ (red solid), $x_{\rm SiII}$ (black dashed), $x_{\rm SiIII}$ (black solid), $x_{\rm OII}$ (orange dashed) and $x_{\rm OIII}$ (orange solid); $x_{\rm CIV}$ (red dotted), $x_{\rm SiIV}$ (black dotted) and $x_{\rm SiV}$ (black dashed-dotted).

by averaging the input physical quantities on all the cells of the plane at the same distance h from cell $(30, 64, 64)$ (see Fig. 11). The results refer to the final time $t_f = 5 \cdot 10^8$ yrs. Figure 12 shows the profiles of the ionization fraction of some selected ions.

The profile of the H and He species is very similar to that of a single Strömgren sphere (see Test 1), with the exception of $x_{\rm HeIII}$, which is always confined in regions very close to the sources and thus is not shown.

In the middle panel C II, C III, Si II, Si III, O II and O III are shown together because they trace the external regions of the two overlapping Strömgren spheres (see Fig. 6). C III, O III and Si III are present for $h < 12$ cells with different ionisation fractions ($x_{\rm OIII} \sim 1$, $x_{\rm CIII} \sim 0.5$ and $x_{\rm SiIII} \sim 0.3$), indicating that these ions have a different sensitivity to the ionising field; this is also in qualitative agreement with the relative trends noticed in Test 1 (see Fig. 6).

In the lower panel $x_{\rm CIV}$, $x_{\rm SiIV}$ and $x_{\rm SiV}$ are shown. Similarly to the species analysed in the previous panel, they present an almost constant value throughout the fully ionised region, with the exception of $x_{\rm SiV}$, which starts declining earlier, in favour of lower ionisation states. The absence of O IV, O V and C V (which reach an ionisation fraction of only a few percent) is consistent with the absence of He III. Compared to the corresponding species in Test 1, here the ionisation fractions are higher due to the larger ionisation rate.

5.2.2 Variations in the source ionisation rates

In this Section we discuss the variations in the results induced by changes in the ionisation rates. These are shown in Figure 13 for some reference species.

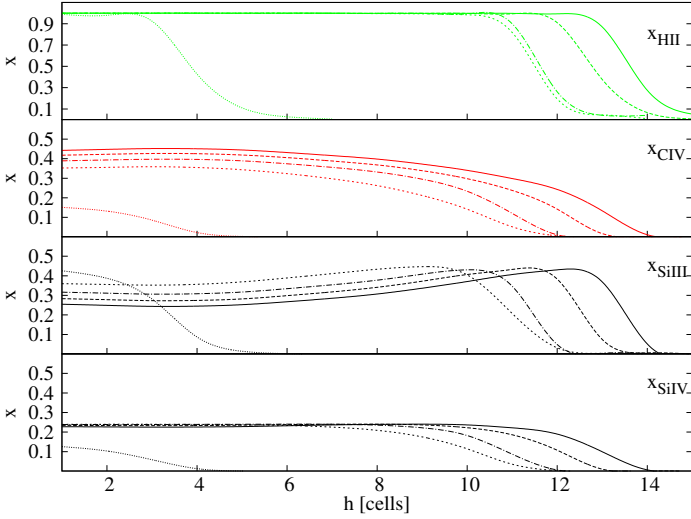First we have decreased the ionisation rates of the two

Figure 13. Ionisation fractions as function of h, evaluated in the plane equidistant from the two sources ($x = 30$) of Test 2 when the source ionisation rate is changed compared to the reference case (see text for details). From the top to the bottom the panels refer to x_{HII}, x_{CIV}, x_{SiIII} and x_{SiIV}. In all panels solid lines refer to the reference case with $\dot{N}_1 = \dot{N}_2 = 9 \cdot 10^{51}$ phot s^{-1}; dashed to $\dot{N}_1 = 9 \cdot 10^{51}$ phot s^{-1} and $\dot{N}_2 = 7 \cdot 10^{51}$ phot s^{-1}; short-dashed to $\dot{N}_1 = 9 \cdot 10^{51}$ phot s^{-1} and $\dot{N}_2 = 3 \cdot 10^{51}$ phot s^{-1}; dashed-dotted to $\dot{N}_1 = \dot{N}_2 = 7 \cdot 10^{51}$ phot s^{-1}; dotted to $\dot{N}_1 = \dot{N}_2 = 3 \cdot 10^{51}$ phot s^{-1}.

sources simultaneously, maintaining the symmetry of the problem, i.e. using $\dot{N}_1 = \dot{N}_2 = 7 \cdot 10^{51}$ phot s^{-1} and $3 \cdot 10^{51}$ phot s^{-1}, the latter being the minimum ionising rate allowing for an overlap of the two HII regions. We have then decreased the ionisation rate of only one source, while maintaining $\dot{N}_1 = 9 \cdot 10^{51}$ phot s^{-1}. As expected, the extent of the fully ionised region (upper panel) decreases with decreasing total ionisation rate. A similar trend is observed also in the profile of the other species, which changes smoothly with decreasing ionisation rate. Compared to the behaviour of x_{HII} though, these differ in that also the amount of ionisation decreases. Remarkably, x_{SiIV} seems to be insensitive to small variations of the ionisation rates, at least in the inner parts of the HII region. This suggests that other species would be more suitable to give indications on the characteristics of the sources.

By comparing qualitatively the results with those in Figure 6 we can conclude that `CRASH3` produces the predictable behaviour for the ions also when more than one source is present and that it is sensitive to small changes in the source ionisation rates. This is very important for realistic applications of the code.

5.2.3 Variations in the source spectra

In this Section we study the variations induced by changes in the temperatures T_1 and T_2 of the black-body spectra. The source ionisation rates are set to the reference value $\dot{N}_1 = \dot{N}_2 = 9 \cdot 10^{51}$ phot s^{-1}. The results in terms of distribution of some reference ionisation fractions are shown in Figure 14.

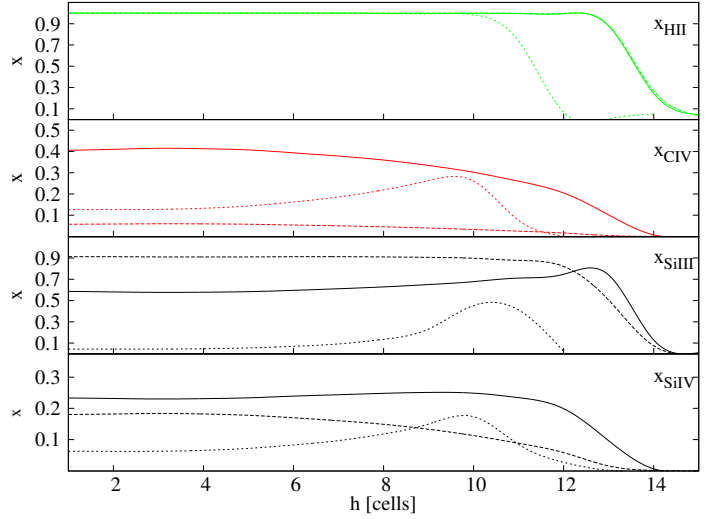In the top panel the H II I-front is identical in the cases

Figure 14. Ionisation fractions as function of h, evaluated in the plane equidistant from the two sources ($x = 30$) of Test 2 when the source spectrum is changed compared to the reference case (see text for details). From the top to the bottom the panels refer to x_{HII}, x_{CIV}, x_{SiIII} and x_{SiIV}. In all panels solid lines refer to the reference case with $T_1 = T_2 = 10^5$ K; the dashed to $T_1 = T_2 = 5 \cdot 10^4$ K and the short-dashed to $T_1 = T_2 = 5 \cdot 10^5$ K.

$T_1 = T_2 = 5 \cdot 10^4$ K and $T_1 = T_2 = 10^5$ K, while it recedes significantly for $T_1 = T_2 = 5 \cdot 10^5$ K. This is because by increasing the temperature from $5 \cdot 10^4$ K to 10^5 K, most of the photons still have $E < E_{HeII}$ and get preferentially absorbed by hydrogen because of its higher abundance. For these two cases x_{HeII} (which is not plotted here) has a profile very similar to that of x_{HII}, with the only difference that it slightly increases with increasing temperature because more photons have $E > E_{HeI}$. On the other hand, when the temperature of the black-body spectra is increased to $5 \cdot 10^5$ K, most of the photons have an energy in the vicinity of E_{HeII}, causing a drop in x_{HII} and x_{HeII} and the appearance of x_{HeIII} (which is not plotted here), which was missing in the other cases, being relegated only in the immediate surroundings of the sources.

While for $T_1 = T_2 = 5 \cdot 10^4$ K there is hardly any C IV available because of the lack of enough photons with $E > E_{CIII}$, as the spectrum temperature increases so does x_{CIV}. Increasing the black-body temperature further, and thus shifting the peak of the black-body spectrum to higher frequencies, brings a drop in x_{CIV}, which is balanced by an equal increment of x_{CV} (which is not shown in this plot).

Unlike in the previous tests, in this case both Si III and Si IV show remarkable changes by varying the spectrum temperature. While x_{SiIII} keeps decreasing as the temperature increases and higher ionisation states are favoured, x_{SiIV} increases from $T_1 = T_2 = 5 \cdot 10^4$ K to $T_1 = T_2 = 10^5$ K, while it decreases when $T_1 = T_2 = 5 \cdot 10^5$ K, similarly to x_{CIV}.

Also in this case we can conclude that `CRASH3` is very sensitive to changes in the spectrum of the ionising sources.

We have verified that a similar conclusion applies when only one of the two source temperature is changed or when we have adopted a power-law rather than a black-body spectrum.
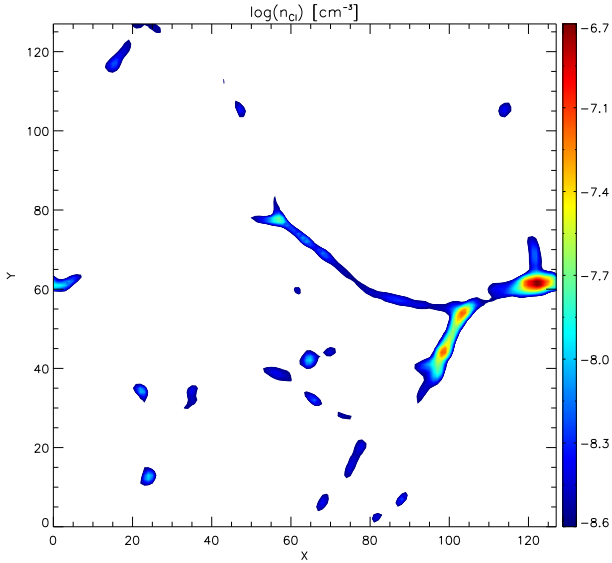
Figure 15. Slice cut through the simulation box showing the initial distribution of $\log(n_{\mathrm{CI}}) \,[\mathrm{cm}^{-3}]$ in Test 3.
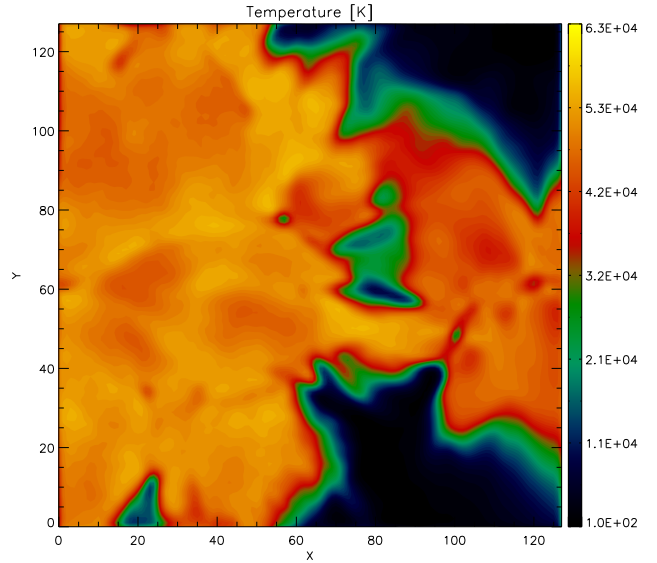

Figure 16. Slice cut through the simulation box showing the distribution of the gas temperature T in the same slice of Figure 15 at the time $t = 5 \cdot 10^4$ yrs in Test 3.

5.3 Test 3: radiative transfer on a cosmological density field enriched by metals

In this Section we present an extension of the Test 4 proposed in the Cosmological Radiative Transfer Comparison Project (Iliev et al. 2006a). The original test set-up has been adopted, but we have extended the ICs to include He, C, O and Si. For reference, the box size is $L_b = 0.5h^{-1}\mathrm{Mpc}$ comoving, $h = 0.72$, $N_c = 128$, the simulation duration is set to $t_f = 4 \cdot 10^5$ yrs, starting at redshift $z = 9$. The cosmological evolution of the box is disabled and the simulation starts with a neutral gas at initial temperature $T = 100$ K.

The H and He fractions are the same as in Test 1. 16 point sources are present in the box with a black-body spectrum at $T = 10^5$ K. The sampling of the spectrum is done with 91 frequencies, to reach the accuracy established in our Test 1. Finally, we have used 10^8 packets to ensure a good convergence as done in MCK09. It is important to note that the aim of this test is to show how the `CRASH3` pipeline is applied to a realistic density configuration and the rich set of information provided by it, and it is not meant to quantitatively reproduce observational results.

Differently from the previous tests in which we populated the full computational volume with metals, here we assign a metallicity of $Z_g = \Delta \cdot 0.0064 Z_\odot$ to those cells with an overdensity $\Delta = \rho/\langle\rho\rangle > 10$. This results in about 5 percent of metal enriched cells. The number density of C, O and Si relative to the hydrogen are the same ones introduced at the beginning of the Test Section.

In Figure 15 the distribution of the C I number density is shown in a slice of the simulation box containing the brightest source, located within the densest region in the computational volume. The distribution of Si I and O I is the same, with $n_{\mathrm{SiI}} = 0.142 \cdot n_{\mathrm{CI}}$ and $n_{\mathrm{OI}} = 2 \cdot n_{\mathrm{CI}}$. By con-

struction, most of the metals are concentrated in the vicinity of the sources and in general in the highest density regions.

As shown in Figure 9 of Test 1, gas with metallicity $Z_g > 0.1 Z_\odot$ starts to cool with different efficiency depending on the distance from the illuminating source (see comments in the Section), while for $Z_g > 0.64 Z_\odot$ the cooling is relevant at every distance from the source. In the box of this Test, cells with $\Delta > 100$, are only 0.012 percent of the total number, while cells with $\Delta > 50$ are about 4 percent. We then expect the effect of metal cooling to be negligible on the global ionisation status of the medium and we ignore it in discussing the results. In realistic 3D simulations the metal cooling should be carefully accounted for in all the cells with $Z_g > 0.1 Z_\odot$, because it acts differently depending on the gas metallicity and the RT effects shaping the field. The statistical effects of the metal cooling will be analysed with care in future applications in the context of physically motivated enrichment patterns.

To better understand the distribution of the metal ionisation species discussed in the following, in Figure 16 we show the distribution of gas temperature in the same slice as above at a time $t = 5 \cdot 10^4$ yrs. Black regions ($T \sim 100$ K) correspond to areas not reached by the radiation field, the green color clearly traces the He II ionisation fronts at a typical temperature $T \sim 2 \cdot 10^4$ K, while the red/orange is associated to regions at $T \sim 4 \cdot 10^4$ K, dominated by H II and He II. Finally, warmer, yellow regions correspond to areas where there is also substantial He III.

The distribution of some reference metal species is shown in Figure 17 across the same slice. While in the vicinity of the brightest source C V is present in large quantities, with x_{CV} as high as 1, only small traces are visible further away. On the other hand, these regions are typically rich in C III, showing a qualitative behaviour similar to the one
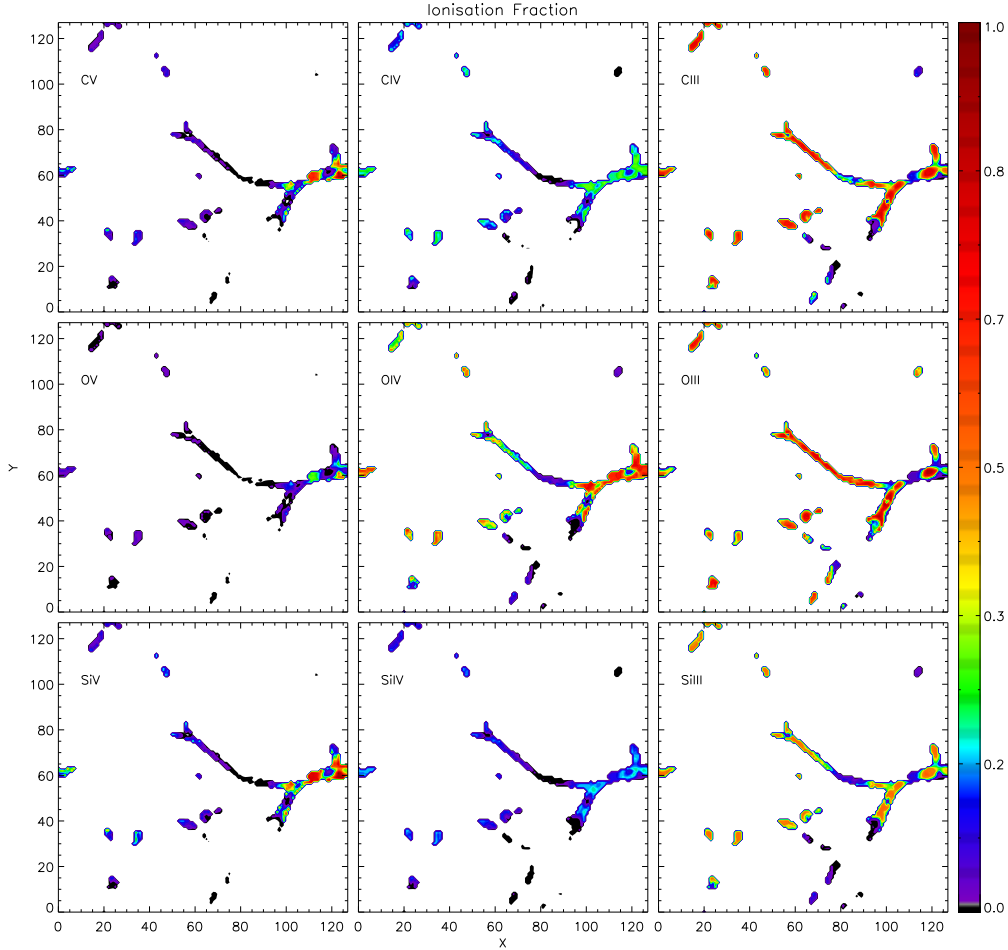
Figure 17. Slice cut through the simulation box showing the distribution of (from left to right and from top to bottom): x_{CV}, x_{CIV}, x_{CIII}, x_{OV}, x_{OIV}, x_{OIII}, x_{SiV}, x_{SiIV} and x_{SiIII}. The slice shown is the same of the previous Figures at the time $t = 5 \cdot 10^4$ yrs in Test 3.

discussed in Test 1, where C V and C III are complementary species. Consistently with the same Test 1, C IV is present everywhere along the filaments with relatively low abundances. Regions with fractions close to zero are those which have not been reached by ionising radiation (see Fig. 16). A similar behaviour is observed for O, with O V present in very small traces only in the vicinity of the brightest source, O IV extending a bit further away along the filaments and O III being present in substantial amounts elsewhere. Finally, while there are only traces of Si IV, x_{SiV} is as high as 1 in the vicinity of the source and Si III is present in modest quantities everywhere.

While it is not possible to make a quantitative comparison with Test 1, the qualitative results in terms of ionisation fractions at a given distance from the brightest source are in good agreement, with the highest ionisation levels present only in the close proximity of the source and the lower ionisation levels present everywhere along the filaments hit by the ionising radiation.

Similarly to what done in Section 5.1.4, we have investigated the impact on the evaluation of metal ionisation states

of photons with $E < 13.6$ eV by extending the spectrum to to energies lower that 13.6 eV down to E_{SiI}. In Figure 18 the differences in ionisation fractions ($\Delta x_i = x_{i,E_{SiI}} - x_{i,E_{HI}}$) computed in the two set-ups are reported for the same ions of Figure 17. As for Test 1, we find that where $x_{HII} \sim 1$ the agreement between the case with and without the inclusion of the low energy tail is excellent in most of the metal enriched domain. x_{OIV} and x_{OIII} present an average discrepancy of about 13%, with a maximum of $\sim 40\%$ confined in few cells where the ionisation fractions are relatively low (i.e. below $\sim 30\%$). For higher x the agreement is excellent, reflecting the results in Section 5.1.4, where the largest discrepancies were observed in correspondence of those cells in which the abundance of the different species was raising or declining. On the other hand x_{OV} always shows a good agreement between the two cases. The Si and C ionisation fractions present a maximum discrepancy below 10% for their higher (i.e. IV and V) ionisation species, while it raises to $\sim 40\%$ for x_{CIII} and x_{SiIII}. Also for these species only few cells have such large discrepancies.

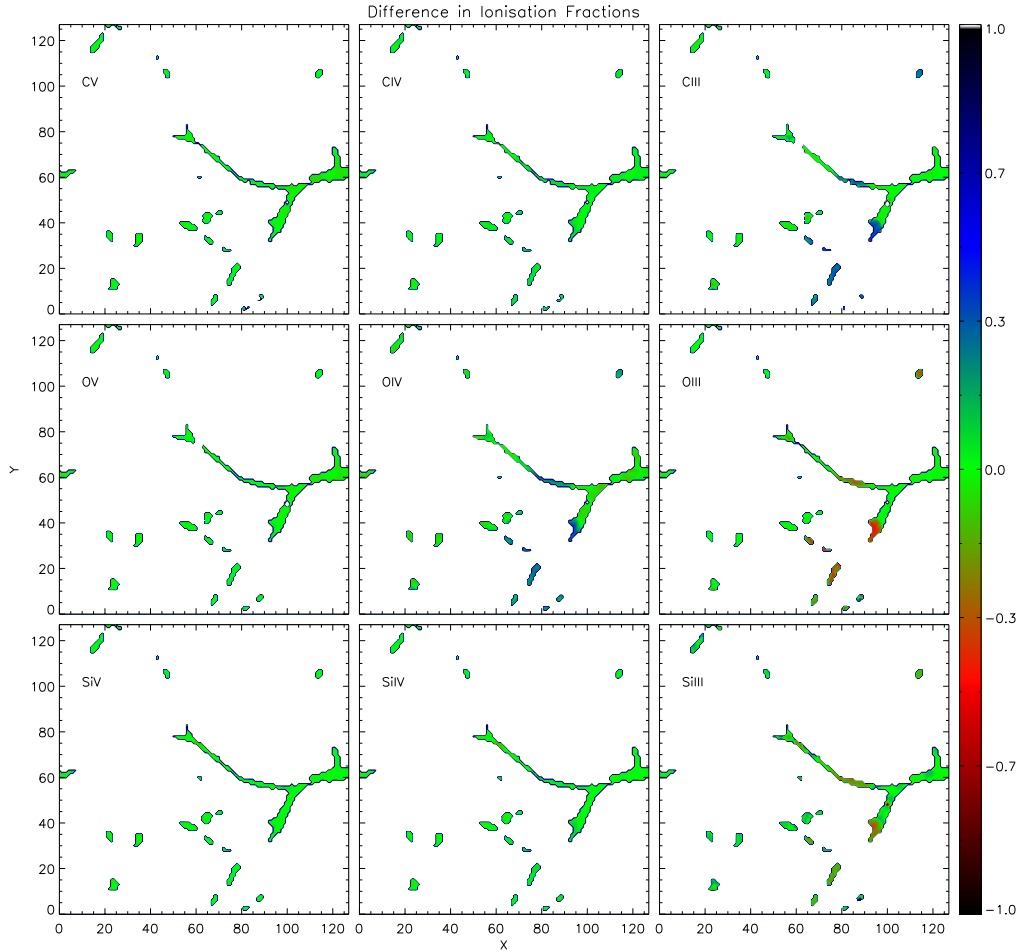In general we can conclude that, similarly to what seen

Figure 18. Slice cut through the simulation box showing the distribution of the differences in ionisation fractions obtained in Test 3 with the reference source spectrum and with a spectrum extending to a lower ionising energy of E_{SiI} ($\Delta x_i = x_{i,E_{\mathrm{SiI}}} - x_{i,E_{\mathrm{HI}}}$; see text for more details). From left to right and from top to bottom the panels refer to the species: C V, C IV, C III, O V, O IV, O III, Si V, Si IV and Si III. The slice shown is the same of the previous Figures at the time $t = 5 \cdot 10^4$ yrs.

in Test 1, the extension of the spectrum to energies lower than 13.6 eV results in some discrepancies in the evaluation of the metal ionisation fractions. Such discrepancies are limited to some of the metal ions (especially the lowest ionisation states) and are largely due to a number of physical processes which are neglected (see footnote of Test 1 and the discussion in Section 5.1.4). In the selected slice, they are also confined to a small number of cells typically located far from the ionising sources. As a reference, the percentage of metal enriched cells which present a discrepancy larger than 5%, 10%, 25% and 50% in the visualised species is 19.3%, 9.6%, 4.2% and 0.6%, respectively.

6   CONCLUSIONS

In this paper we presented `CRASH3`, the latest release of the 3D radiative transfer code `CRASH`. In its current implementation `CRASH3` integrates into the reference algorithm the

code `Cloudy` to evaluate the ionisation states of metals, self-consistently with the radiative transfer through the most abundant species, i.e. H and He. The feedback of the heavy elements on the calculation of the gas temperature is also taken into account, making of `CRASH3` the first 3D code for cosmological applications which treats self-consistently the radiative transfer through an inhomogeneous distribution of metal enriched gas with an arbitrary number of point sources and/or a background radiation. It should be noted that the algorithm is based on the assumption that metals do not contribute to the gas optical depth, which is valid in typical configurations of cosmological interest, as e.g. in the IGM. On the other hand, the code is not suitable for applications in which metallicities $\gtrsim Z_\odot$ are involved.

The pipeline has been tested in idealized configurations, such as the classic Strömgren sphere, albeit enriched with heavy elements, as well as in a more realistic case of multiple sources embedded in a polluted cosmic web, which shows the rich set of information provided by the metal ionisation

states. Through these validation tests the new method has been proved to be numerically stable and convergent with respect to a number of parameters.

The dependence of the results on e.g. the source characteristics (spectral range and shape, intensity), the metal composition, the gas number density and metallicity has been investigated. Despite the difficulty in testing quantitatively the results, we find that the qualitative behaviour is consistent with our expectations.

In conclusion, `CRASH3` is an excellent code to simulate the evolution of various species in a low metallicity gas illuminated by an ionising radiation, which can be modelled both as a background radiation and point sources. `CRASH3` will then be an invaluable tool to investigate the interpretation of e.g. metal absorption lines in quasars' spectra or fluctuations in the UVB, in more detail, with a better modelling of the relevant physical processes and with a higher accuracy than done before. These applications are topics for further investigations.

References

Adelberger K.L., Shapley A.E., Steidel C.C., Pettini M., Erb D. K., Reddy N.A., 2005. ApJ, 629, 636

Allen M. G., Groves B. A., Dopita M. A., Sutherland R. S., Kewley L. J., 1998, ApJS, 178, 20A

Aracil, B., Petitjean, P., Pichon, C., & Bergeron, J. 2004, A&A, 419, 811

Baek S., Semelin B., Di Matteo P., Revaz Y. & Combes F., 2010, A&A, 523A, 4B

Becker G.D., Rauch M., Sargent W.L.W., 2009, ApJ, 698, 1010

Becker G.D., Sargent W.L.W., Rauch M., Calverley, A., 2011, ApJ, 735, 93B

Bolton, J.S., & Viel, M. 2011, MNRAS, 414, 241

Boksenberg A., Sargent W.L.W., Rauch M., 2003, arXiv:astro-ph/0307557

Cen R., Bryan G., 2001, ApJ, 546, 81

Ciardi B., Ferrara A., Marri S., Raimondo G., 2001, MNRAS, 324, 381

Ciardi B, Stoehr F., White S.D.M., 2003a, MNRAS, 343, 1101

Ciardi B., Ferrara A., White S.D.M., 2003b, MNRAS, 344, L7

Ciardi B., Bolton J., Maselli A., Graziani L., 2011, MNRAS, 423, 558

Cooksey K.L., Prochaska J.X., Thom C., Chen H.-W., 2011, ApJ 729,87.

Cowie, L.L., Songaila, A. 1998, Nature 394,44

Dayal, P., Maselli A., Ferrara A., MNRAS, 2011, 430,380

Dopita M.A., Sutherland R.S., 2003, Astrophysics of the diffuse universe, Berlin, New York: Springer, 2003. Astronomy and Astrophysics Library ISBN 3540433627

Draine B.T., 2011, Physics of the Interstellar and Intergalactic Medium, Princeton University Press

Dubois Y., Teyssier R., 2007, EAS Publications Series, 24, 95

Ellison, S.L., Songaila, A., Schaye, J., & Pettini, M. 2000, AJ, 120, 1175

Ercolano B., Barlow M. J., Storey P. J. & Liu X.-W., 2003, MNRAS, 340, 1136

Ferland G.J., Korista K.T., Verner D.A., Ferguson J.W., Kingdon J.B., Verner, & E.M. 1998, PASP, 110, 761

Ferland G.J., 2003, Ann. Rev. Astro. Astrophys., 41, 517

Ferrara A., Pettini M. & Shchekinov Y., 2000, MNRAS, 319, 519

Furlanetto S. R., Loeb A., 2003, ApJ, 588, 18

Furlanetto S.R., 2009, ApJ, 703, 702

Gnedin, N.Y., Ostriker J.P., 1997, ApJ 486, 581

Grevesse N., Sauval A. J., 1998, Space Science Reviews, v. 85, Issue 1/2, 161-174

Hellsten U., Davé R., Hernquist L., Weinberg D.H., Katz N., 1997, ApJ, 487, 482

Hubeny I., 2001, ASPC, 247, 197

Iliev I.T., Ciardi B., Alvarez M.A., Maselli A., Ferrara A., Gnedin N.Y., Mellema G., Nakamoto T., Norman M.L., Razoumov A.O., Rijkhorst E., Ritzerveld J., Shapiro P.R., Susa H., Umemura M., Whalen D.J., 2006a, MNRAS, 371, 1057

Iliev I.T., Mellema G., Pen U.L., Merz H., Shapiro P.R., Alvarez M.A., 2006b, MNRAS, 369, 1625I

Iliev I.T., Whalen D.J., Mellema G., Ahn K., Baek S., Gnedin N.Y., Kravtsov A.V., Norman M.L., Raicevic M., Reynolds D.R., Sato D., Shapiro P.R., Semelin B., Smidt J., Susa H., Theuns T., Umemura M., 2009, MNRAS, 400, 1283

Jeeson-Daniel A., Ciardi B., Maio U., Pierleoni M., Dijkstra M., Maselli A., 2012, arXiv:1204.2554

Lu L., 1991, ApJ, 379, 99

Kulkarni V.P., Fall S;M., Lauroesch J.T., et al., 2005, ApJ, 618,68

Madau P., Ferrara A., Rees M.J., 2001, ApJ, 555, 92

Madau P., Haardt F., 2009, ApJL, 693, L100

Maio U., Dolag K., Ciardi B., Tornatore L., 2007, MNRAS, 379, 963M

Maio U., Ciardi B., Dolag K., Tornatore L., Khochfar S., 2010, MNRAS, 407, 1003M

Maio U., Khochfar S., Johnson J. L., Ciardi B., 2011, MNRAS, 414, 1145M

Maselli A., Ferrara A., Ciardi B., 2003, MNRAS, 345, 379

Maselli A., Ferrara A., 2005, MNRAS, 364, 1429

Maselli, A., Gallerani, S., Ferrara, A., Choudhury, T. R., 2007, MNRAS, 376, L34-L38

Maselli A., Ciardi B., Kanekar A., 2009, MNRAS, 393, 171 (MCK09)

Maselli A., Ferrara A., Gallerani S., 2009, MNRAS, 395, 1925

McQuinn M., Lidz A., Zaldarriaga M., Hernquist L., Hopkins, P.F., Dutta S., Faucher-Giguère C., 2009, ApJ, 694, 842

Meiksin A.A., White M., 2003, MNRAS, 342, 1205

Meiksin A.A., 2009, Rev. Mod. Phys., 81, 1405

Meyer, D.M., & York, D.G. 1987, ApJ, 315, 5

Oh P.S., 2002, MNRAS, 336, 1021

Oppenheimer B.D., Davé R., 2006, MNRAS, 373, 1265

Oppenheimer, B.D., Davé R., Finlator K., 2009, MNRAS, 396, 729

Oppenheimer, B.D., Davé R., Katz N., Kollmeier J.A., Weinberg D. H., 2012, MNRAS, 420, 829

Osterbrock D.E. & Ferland G.J., 2006, Astrophysics of Gaseous Nebulae and Active Galactic Nuclei, Second Edition (Sausalito, California: University Science Books).

Partl A. M., Maselli A., Ciardi B., Ferrara A., Müller V., 2011, MNRAS, 414,428

Petitjean P., 2001, ApSS, 227S: 517-525

Petitjean P., in V. Hill, Fran ç ois, F., & Primas F., 2005 IAU Symposium 228

Pettini M., Ellison S.L., Steidel C.C., Bowen D.V., 1999, ApJ, 510, 576.

Pieri, M.M. & Haenhelt, M. G. 2004, MNRAS, 347, 985

Pierleoni M., Maselli A., Ciardi B., 2009, MNRAS, 393, 872P

Rauch, M., Haehnelt M.G., Steinmetz M., 1997, ApJ, 481, 601

Ryan-Weber E. V., Pettini M., Madau P., Zych B. J., 2009, MNRAS, 395, 1476

Scannapieco E., Ferrara A., & Madau P., 2002, ApJ, 574, 590

Scannapieco, E., Pichon; C., Aracil, B., Petitjean, P., Thacker, R.J., Pogosyan, D., Bergeron, J., & Couchman, H.M.P., 2006, MNRAS, 365, 615

Schaye, J., Rauch, M., Sargent, W.L.W., & ki, T. 2000, ApJ, 541L,1S

Schaye, J., Aguirre, A., Kim, T., Rauch, M., & Sargent, W.L.W. 2003, ApJ, 596, 768

Schaye J., Dalla Vecchia C., Booth C. M., et al., 2010, MNRAS, 402, 1536

Shen S., Wadsley J., Stinson G., 2010, MNRAS, 407, 1581

Simcoe R.A., Sargent W.L.W, Rauch M., 2004, ApJ, 606, 92

Simcoe R.A., Cooksey K.L., Matejek M., Burgasser A.J., Bochanski J., Lovegrove E., Bernstein R.A., Pipher J.L., Forrest W.J., McMurtry C., Fan X., O'Meara J., 2011, ApJ, 743, 21S

Smith B., Sigurdsson S., Abel T., 2008, MNRAS, 385, 1443S

Songaila A., Cowie, L.L. 1996, AJ 112, 335.

Songaila, A., 2001, ApJ, 561, L153

Songaila A., 2005, AJ, 130, 1996

Steidel C.C., 1990, ApJS, 74, 37.

Sutherland R.S., Dopita M.A., 1993, ApJS, 88, 253

Thacker R.J., Scannapieco E., Davis M., 2002, ApJ, 202, 581

Tytler D., Fan X.M., Burles, S., Cottrell, L., Davis, C., Kirkman, D., Zuo, L., 1995, in Meylon G., ed., Proc. ESO Workshop, QSO Absorption lines, Springer, Berlin, 289.

Tornatore L., Borgani S., Viel M., Springel V., 2010, MNRAS, 402, 1911

Trac H., Cen R., 2007, ApJ, 671, 1T

Verhamme A., Schaerer D., Maselli A., 2006, A&A, 460,397

Wiersma R. P. C., Schaye J., Smith B. D., 2009a, MNRAS, 393, 99W

Wiersma R. P. C., Schaye J., Theuns T., Dalla Vecchia C., Tornatore, L., 2009b, MNRAS, 399, 574W
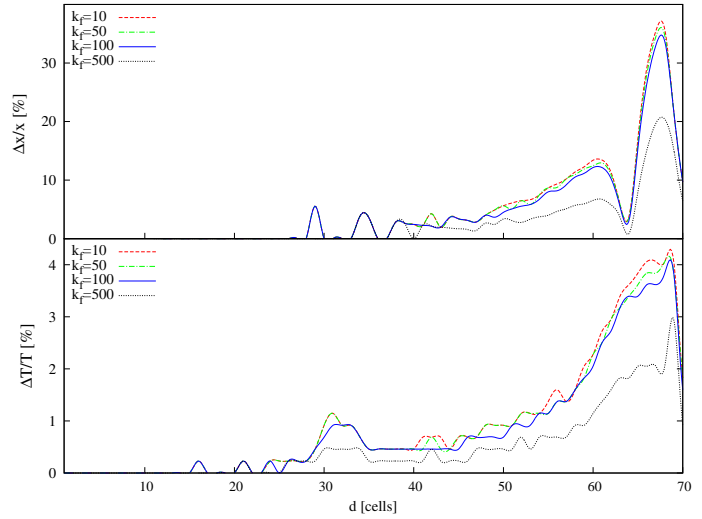
Wiersma R. P. C., Schaye J., Dalla Vecchia C., Booth C. M., Theuns T., Aguirre A., 2010, MNRAS, 409, 132W

Wiersma R. P. C., Schaye J., Theuns T., 2011, MNRAS, 415, 353W

Zuo L., 1992a, MNRAS, 258, 36

Zuo L., 1992b, MNRAS, 258, 45

Figure A1. $\Delta x/x=|x(k_f=1000)-x(k_f)|/x(k_f=1000)$ (**upper panel**) and $\Delta T/T=|T(k_f=1000)-T(k_f)|/T(k_f=1000)$ (**lower**) as a function of the distance d from the source in Test 1 including the feedback from metals. Here x refers to the ionisation fraction x_{CII}. The curves are plotted at the time $t_f = 5 \cdot 10^8$ yrs and refer to a value of $k_f = 10$ (red dashed lines), 50 (green dashed-dotted), 100 (blue solid) and 500 (black dotted).

APPENDIX A: CONVERGENCE TESTS

When the temperature feedback is introduced in the `CRASH3` pipeline (see description of Step 3) k_f times, the RT process is altered. While the gas recombination depends weakly on the temperature and we can expect negligible effects, the numerical convergence of the metal ionisation fractions needs be verified for different values of k_f.

Here we show the results of some tests run to check the convergence of our results with respect to k_f when the metal feedback is enabled.

In Figure A1 we show the profile of the variation of a reference ionisation fraction (x_{CII}) and temperature for Test 1 run with the metal feedback switched on. The lines refer to the final time $t_f = 5 \cdot 10^8$ yrs and to values of $k_f = 10$, 50, 100 and 500. The convergence of the results within the ionised sphere ($d \leqslant 40$ cells) is excellent: even for small values of k_f the relative discrepancies remain within few percent both in the ionisation fraction (top panel) and in the temperature (bottom panel). Numerical oscillations of a few percent (or smaller) in $\Delta x/x$ are present in a handful of isolated cells, but they disappear for $k_f \geqslant 100$.

Closer to the I-front ($d \geqslant 50$), where x_{CII} is very small (i.e. $\leqslant 10^{-4}$), the convergence is worse, in particular in the 2-3 cells encompassing the I-front. This behaviour was expected because, as already discussed in Test 1, the accuracy of our scheme is diminished in the outer regions of the

ionised bubble, where the `Cloudy` computation is not always convergent. It should be noticed, however, that x_{CII} presents one of the worse behaviours and higher ionisation states are more numerically stable. We have checked that the convergence is similar also at earlier times, when the ionised sphere has not reached an equilibrium configuration. Other species show a similar dependence on k_f. For example, x_{CIV} presents an excellent convergence (of the order of a percent) within the ionised region already with $k_f = 10$, while in the proximity of the I-front, where $x_{\mathrm{CIV}} \leqslant 10^{-6}$, it degrades to tens of percent.

The temperature shows an even better behaviour, with a relative convergence of a few percent even in the vicinity of the I-front. Also at earlier times the convergence is never worse than 10%. The oscillations in the curves have the same origin of those in the upper panel.

We should notice that the value of k_f needed to reach a good convergence is likely dependent on the problem at hand. In general, though, we can conclude that we expect a value of $k_f \sim 500$ to be sufficient for most applications which require the feedback of metals on the determination of the gas temperature.